Provided for non-commercial research and education use.
Not for reproduction, distribution or commercial use.

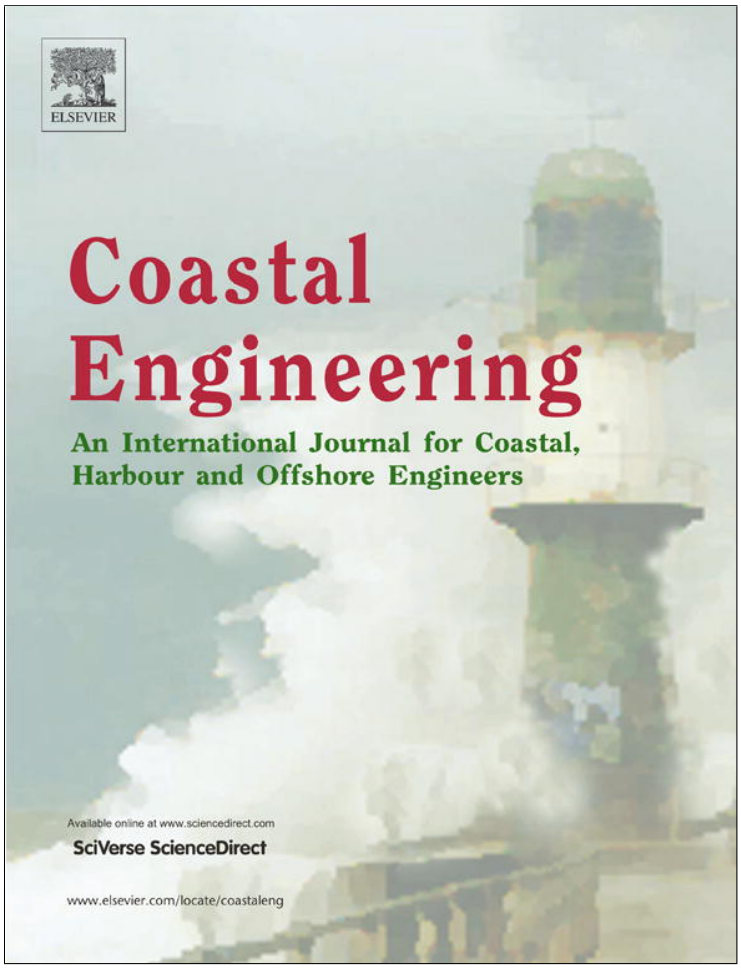

(This is a sample cover image for this issue. The actual cover is not yet available at this time.)

This article appeared in a journal published by Elsevier. The attached copy is furnished to the author for internal non-commercial research and education use, including for instruction at the authors institution and sharing with colleagues.

Other uses, including reproduction and distribution, or selling or licensing copies, or posting to personal, institutional or third party websites are prohibited.

In most cases authors are permitted to post their version of the article (e.g. in Word or Tex form) to their personal website or institutional repository. Authors requiring further information regarding Elsevier's archiving and manuscript policies are encouraged to visit:

http://www.elsevier.com/copyright

Author's personal copy

Coastal Engineering 72 (2013) 1–19

Contents lists available at SciVerse ScienceDirect

Coastal Engineering

journal homepage: www.elsevier.com/locate/coastaleng

An integrated model for the wave-induced seabed response around marine structures: Model verifications and applications

D.-S. Jeng [a,*], J.-H. Ye [a], J.-S. Zhang [b], P.L.-F. Liu [c]

[a] Division of Civil Engineering, University of Dundee, Dundee, DD1 4HN, UK
[b] State Key Laboratory of Hydrology-Water Resources and Hydraulic Engineering, Hohai University, 210098, China
[c] School of Civil and Environmental Engineering, Cornell University, Ithaca, NY 14853, USA

ARTICLE INFO

Article history:
Received 20 May 2011
Received in revised form 27 August 2012
Accepted 28 August 2012
Available online xxxx

Keywords:
Integrated model
Wave–seabed–structure interaction (WSSI)
Porous seabed
Biot's theory
Composite breakwater
Liquefaction

ABSTRACT

In this study, an integrated model (PORO-WSSI II) for wave–seabed–structure interactions (WSSI) is developed by combining (i) the Volume-Averaged Reynolds-Averaged Navier–Stokes (VARANS) equations for wave motions in a fluid domain and the porous media flows in porous structures, and (ii) the dynamic Biot's equations for a porous elastic seabed. The effects of the porous flow in seabed and marine structures, and the fluid exchange at the interface between the fluid domain and solid domain on wave characteristics are considered. The finite difference two-step projection method and the forward time difference method are adopted to solve the VARANS equations. The volume of fluid (VOF) method is applied to track water free-surface. The finite element method and the Generalized Newmark method are respectively adopted for the space discretization and time discretization of the dynamic Biot's equations. A one-way integrating method is developed to integrate the VARANS equations with the dynamic Biot's equations. Several experimental data available in the literature are used to validate the integrated model. An overall agreement between the numerical results and the experiment data indicates that the integrated model developed for the WSSI problem is highly reliable. The integrated model is then applied to investigate the dynamic response of a large-scale composite breakwater on a seabed, and the mechanism of WSSI. Numerical results indicate that there are intensive fluid exchanges between the water body and the seabed and strong seepage forces in the seabed under the ocean wave loading. The excessive upward seepage force leads to the liquefaction of the seabed in the region under wave trough. There is a liquefaction zone in the seabed close to the bottom corner of the rubble mound, which may lead to foundation instability of the composite breakwater. The parametric study indicates that the wave characteristics have a significant impact on the liquefaction properties (depth, width and area).

© 2012 Elsevier B.V. All rights reserved.

1. Introduction

The coastal zone is a unique geological, physical and biological area of vital economic, cultural and environmental value. More than two-thirds of the world's population are concentrated in coastal zones, where the coastline is either central or of great importance to trade, transport, tourism, leisure and the harvesting of marine food. Breakwaters are commonly adopted to protect and enhance the utility of coastlines. For example, the total length of all breakwaters in Japan is 4143 km-one fifth of its coastline (Hsu et al., 2000). In most countries such as the UK and Japan, coastline protection is a national priority. The construction of new breakwaters and the expansion of existing breakwaters involve a major investment. Worldwide, the combined costs for building new breakwaters and maintaining the existing ones are in the order of tens of billions of pounds a year.

Breakwaters are vulnerable to the liquefaction of the seabed foundation, a process that can often lead to a significant degradation of the foundation in as little as a few years after construction and sometimes even result in total collapse (Chung et al., 2006; Franco, 1994; Lundgren et al., 1989; Sumer and Fredsóe, 2002; Zen et al., 1985; Zhang and Ge, 1996). An inappropriate design or maintenance of breakwaters can lead to a catastrophic coastal disaster. A recent example of coastal tragedy due to failure of breakwaters is that of New Orleans during Hurricane Katrina, which caused deaths and personal and economic chaos (Travis, 2005).

The phenomenon of the wave–seabed–structure interactions (WSSI) has a major bearing on this issue and is central to the design of coastal structures such as breakwaters, pipelines and platforms. Numerous studies of wave-induced seabed response have been conducted since the 1970s, involving the investigations of pore pressures, effective stresses, and displacements (Hsu and Jeng, 1994; Madsen, 1978; Mei and Foda, 1981; Okusa, 1985; Yamamoto et al., 1978). Most of them have based on Biot's poro-elastic theory (Biot, 1941). Later, the analytical solutions of dynamic response for a poro-elastic, isotropic seabed under linear wave loading have been developed, in which the inertia effects of the solid and/or pore fluid are included (Jeng and Cha, 2003; Jeng and Rahman, 2000; Jeng et al., 1999). Recently, Ulker et al. (2009)

* Corresponding author.
E-mail address: jengd2@asme.org (D.-S. Jeng).

0378-3839/$ – see front matter © 2012 Elsevier B.V. All rights reserved.
http://dx.doi.org/10.1016/j.coastaleng.2012.08.006

Author's personal copy

further examined the applicable ranges of different approximations. All these investigations have been limited to the dynamic response of the seabed under linear/nonlinear wave loading, without a marine structure.

There have been numerous investigations for the interactions of the wave–seabed around marine structures, based on Biot's poro-elastic theory. Among these, Mase et al. (1994) developed a FEM numerical model to investigate the wave-induced pore water pressures and effective stresses under standing waves in a sand seabed and in the rubble mound foundation of a composite caisson-type breakwater based on Biot's consolidation equations. Later, Mizutani and Mostafa (1998) and Mostafa et al. (1999) developed a BEM–FEM combination numerical model to investigate the wave–seabed–structure interaction. In their models, the Poisson's equation is used to govern the irrotational wave field for an incompressible, inviscous fluid; and the poro-elastic Biot's consolidation equations are used to govern the porous seabed and structures. Jeng et al. (2001) developed a 2D generalized FEM numerical model (GFEM–WSSI) to investigate the wave-induced pore pressure under a linear wave around a composite breakwater located at a finite, isotropic and homogeneous seabed. Recently, Ulker et al. (2010) investigated the dynamic response and instability of the seabed around a caisson breakwater under standing waves with a FEM numerical model,which is developed by considering the acceleration of relative displacements between the solid and pore fluid particles. However, all these models have been based on the potential flow theory for wave models.

In addition to the potential flow, models combining the Reynolds-Averaged Navier–Stokes equations (RANS) for wave field and the Volume-Averaged Reynolds-Averaged Navier–Stokes (VARANS) equations for the porous flow in a porous medium have been developed to examine the phenomenon of the wave propagation around marine structures (Huang et al., 2003; Hur et al., 2008, 2010; Lara et al., 2006; Liu et al., 1999; Shao, 2010). The major advantage of using RANS and VARANS instead of the potential flow for wave modeling is the capacity of capturing wave breaking, turbulence and detailed information of bottom boundary layers. In these models, the pressure, flow field in whole computational domain, and the flux at the interface between the porous seabed/marine structures and the seawater, are all continuous. However, the variations of effective stresses in the seabed and marine structures cannot be determined.

In this study, to improve the capability of modeling the mechanism of WSSI, an integrated model (PORO-WSSI II) will be proposed. In Section 2, the wave and seabed sub-models will be outlined first. The VARANS equations are used for the description of the wave motion and the porous flow in the seabed and marine structures. The dynamic Biot's theory is then used to describe the mechanical behavior of the porous seabed. Furthermore, a one-way integrating algorithm, based on the radial point interpolation method, is adopted to link two models through the continuity of the pressure and velocity/flux at the interface between the seabed/marine structures and sea water. In Section 3, the present model will be validated with the existing experimental data. Then, a series of parametric studies for the wave-induced dynamic seabed response and liquefaction zones around the composite breakwaters will be presented in Section 4. Finally, several key conclusions will be summarized.

2. Numerical model

The proposed integrated numerical model consists of two sub-models: the wave and seabed models. The wave model is used for generating waves and describing their propagation in a viscous fluid. The seabed model is used to determine the seabed responses to the waves, including the pore pressure, soil displacements and effective stresses. A one-way integrating algorithm is adopted to integrate both models together. Unlike most previous investigations in which Poisson's equations or Laplace's equations, and the quasi-static Biot's consolidation equations are used, in this study, the VARANS equations and the dynamic Biot's equations are used to govern the wave motions and porous flows in the porous seabed and marine structures, and the dynamic mechanical behaviors of the seabed and marine structures. Due to the fact that the flow fields outside and inside the porous medium are coupled in the wave model, both the pressure and the flow velocity are continuous in the entire computational domain, especially at the interfaces between the seabed, marine structures and the sea water. In the dynamic Biot's equations, the accelerations of the solid and pore water are included.

2.1. Wave model

In this study, the flow field inside and outside of the porous media is determined by solving the VARANS equations (Hsu and Liu, 2002), which are derived by integrating the RANS equations over the control volume. The mass and momentum conservation equations can be expressed as:

$$\frac{\partial\left\langle \overline{u}_{fi}\right\rangle}{\partial x_i}=0 \tag{1}$$

$$\frac{\partial\left\langle \overline{u}_{fi}\right\rangle}{\partial t}+\frac{\left\langle \overline{u}_{fj}\right\rangle}{n(1+c_A)}\frac{\partial\left\langle \overline{u}_{fi}\right\rangle}{\partial x_j}=\frac{1}{1+c_A}\left[-\frac{n}{\rho_f}\frac{\partial\langle\overline{p}\rangle^f}{\partial x_i}-\frac{\left\langle\overline{\partial u'_{fi}u'_{fj}}\right\rangle}{\partial x_j}+\frac{1}{\rho_f}\frac{\partial\left\langle\overline{\tau}_{ij}\right\rangle}{\partial x_j}+ng_i\right]-\frac{\langle\overline{u}_i\rangle}{1+c_A}\left[\frac{\alpha(1-n)^2}{n^2d_{50}^2}+\frac{\beta(1-n)}{n^2d_{50}}\sqrt{\left\langle\overline{u}_{f1}\right\rangle^2+\left\langle\overline{u}_{f2}\right\rangle^2}\right] \tag{2}$$

where u_{fi} is the flow velocity, x_i is the Cartesian coordinate, t is the time, ρ_f is the water density, p is the pressure, τ_{ij} is the viscous stress tensor of mean flow, g_i is the acceleration due to gravity, and n and d_{50} are the porosity and the equivalent mean diameter of the porous material. c_A denotes the added mass coefficient, calculated by $c_A=0.34(1-n)/n$. In Eq. (2), α and β are empirical coefficients associated with the linear and nonlinear drag forces, respectively. Through the fitting and regression of a wide range of experiment data, Liu et al. (1999) suggested that the $\alpha=200$ and $\beta=1.1$ for the porous flow. Recently, Lara et al. (2011) recommends two nonlinear relations relating the empirical coefficients α and β to the porosity n and mean particle size d_{50}: $\alpha=4409.22d_{50}$, $\beta=12.27\frac{n^3}{(1-n)^{1.5}}d_{50}^{-0.1075}$.

The influence of turbulence fluctuations on the mean flow, denoted as $\langle u'_{fi}u'_{fj}\rangle$, is obtained by solving the volume-averaged $k-$ turbulence model. "$\langle\rangle$" and "$\langle\rangle^f$" stand for Darcy's volume averaging operator and the intrinsic averaging operator, respectively, which are defined as:

$$\langle a\rangle=\frac{1}{V}\int_{V_f}a\,dv,\text{ and }\langle a\rangle^f=\frac{1}{V_f}\int_{V_f}a\,dv \tag{3}$$

where V is the total averaging volume, and V_f is the portion of V that is occupied by the fluid. The relationship between the Darcy's volume averaging operator and intrinsic volume averaging is $<a>=n<a>^f$.

In the VARANS equations, the interfacial forces between the fluid and solids have been modeled according to the extended Forchheimer relationship, in which both linear and nonlinear drag forces between the pore water and the skeleton of the porous structures are included in the last term of Eq. (2). More detailed information on the RANS and VARANS models are available in Lin and Liu (1998) and Hsu and Liu (2002).

2.2. Seabed model

In this paper, the dynamic Biot's equations (so-called "$u-p$" approximation) proposed by Zienkiewicz et al. (1980) are used to describe the dynamic response of the porous seabed under wave loading. Unlike previous quasi-static soil behaviors (Biot, 1941), the accelerations of the pore water and soil particles are considered in the present seabed

Author's personal copy

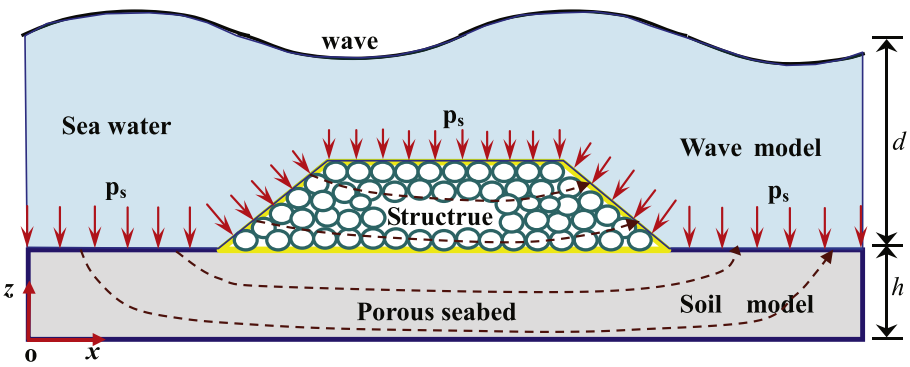

Fig. 1. The sketch of the integration between the wave model and the soil model.

model, but the relative displacements of the pore fluid to soil particles are ignored, which leads to

$$G\nabla^2 u_s + \frac{G}{1-2\mu_s}\frac{\partial \varepsilon_s}{\partial x} = -\frac{\partial p_s}{\partial x} + \rho\frac{\partial^2 u_s}{\partial t^2}, \tag{4}$$

$$G\nabla^2 v_s + \frac{G}{1-2\mu_s}\frac{\partial \varepsilon_s}{\partial z} + \rho g = -\frac{\partial p_s}{\partial z} + \rho\frac{\partial^2 v_s}{\partial t^2}, \tag{5}$$

$$k_s\nabla^2 p_s - \gamma_w n\beta\frac{\partial p_s}{\partial t} + k_s\rho_f\frac{\partial^2 \varepsilon_s}{\partial t^2} = \gamma_w\frac{\partial \varepsilon_s}{\partial t}, \tag{6}$$

where (u_s, v_s) = the soil displacements in the horizontal and vertical directions, respectively; n = soil porosity; μ_s = Poisson's ratio; p_s = the pore water pressure; $\rho = \rho_f n + \rho_s(1-n)$ is the average density of the porous seabed; n = porosity of the porous medium ρ_s = solid density; k_s = the Darcy's permeability; g = the gravitational acceleration and γ_ω is the unit weight of fluid. G is the shear modulus of soil, and μ_s is the Poisson's ratio. In Eq. (6), the compressibility of the pore fluid (β) and the volumetric strain ($_s$) are defined as

$$\beta = \left(\frac{1}{K_f} + \frac{1-S_r}{p_{w0}}\right), \quad \text{and} \quad \epsilon_s = \frac{\partial u_s}{\partial x} + \frac{\partial v_s}{\partial z}, \tag{7}$$

where S_r = the degree of the saturation of the seabed, p_{w0} = the absolute static pressure and K_f = the bulk modulus of pore water.

Based on the generalized Hooke's law, the relationship between the elastic incremental effective stresses and soil displacements are given by

$$\sigma'_{sx} = 2G\left[\frac{\partial u_s}{\partial x} + \frac{\mu_s\epsilon_s}{1-2\mu_s}\right], \sigma'_{sz} = 2G\left[\frac{\partial v_s}{\partial z} + \frac{\mu_s\epsilon_s}{1-2\mu_s}\right], \tau_{sxz} = G\left[\frac{\partial u_s}{\partial z} + \frac{\partial v_s}{\partial x}\right] \tag{8}$$

where σ'_{sx} and σ'_{sz} = effective normal stresses in the horizontal and vertical directions, respectively; and τ_{sxz} = shear stress;

To solve the pore pressures (p_s) and soil displacements (u_s and v_s) in Eqs. (4)–(6), the following boundary conditions are imposed:

- *Boundary conditions at the seabed surface* (*SBC*): it is commonly accepted that vertical effective normal stress and shear stresses vanish, and the pore pressure is equal to the wave pressure at the seabed surface, i.e.,

$$p_s = P_b, \quad \sigma'_{sz} = 0 \quad \text{and} \quad \tau_{sxz} = 0 \quad \text{at} \quad z = h \tag{9}$$

  where P_b is the dynamic wave pressures obtained from the wave model.
- *Boundary conditions at the seabed bottom* (*BBC*): for the soil resting on

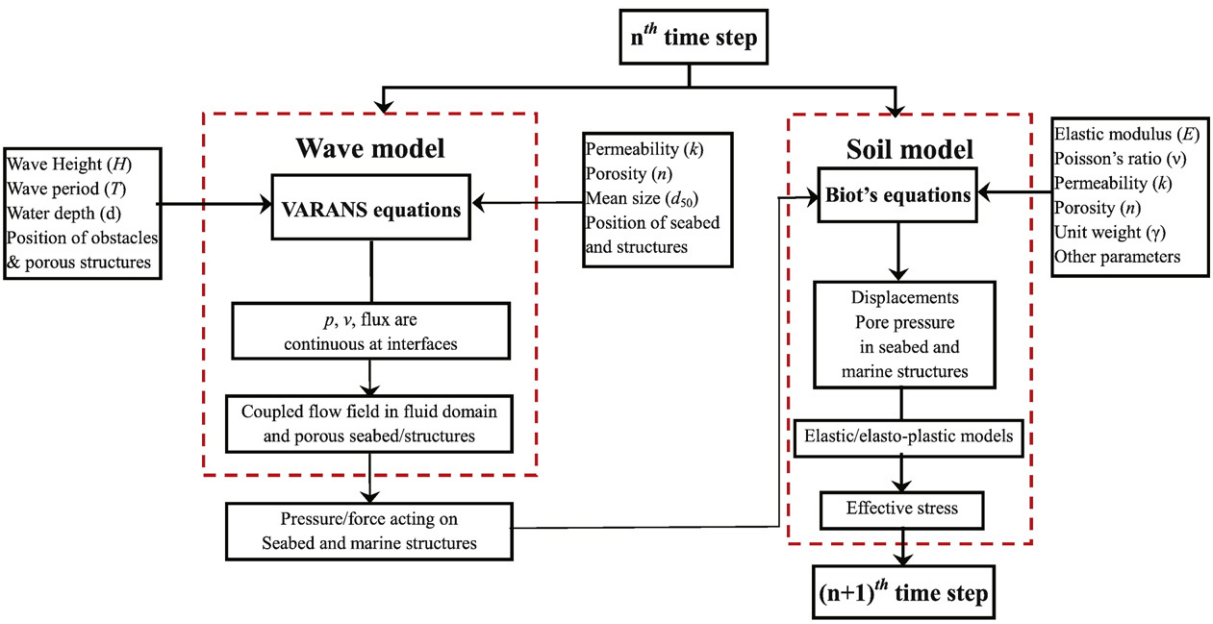

Fig. 2. The integrating process adopted in PORO-WSSI II.

Author's personal copy

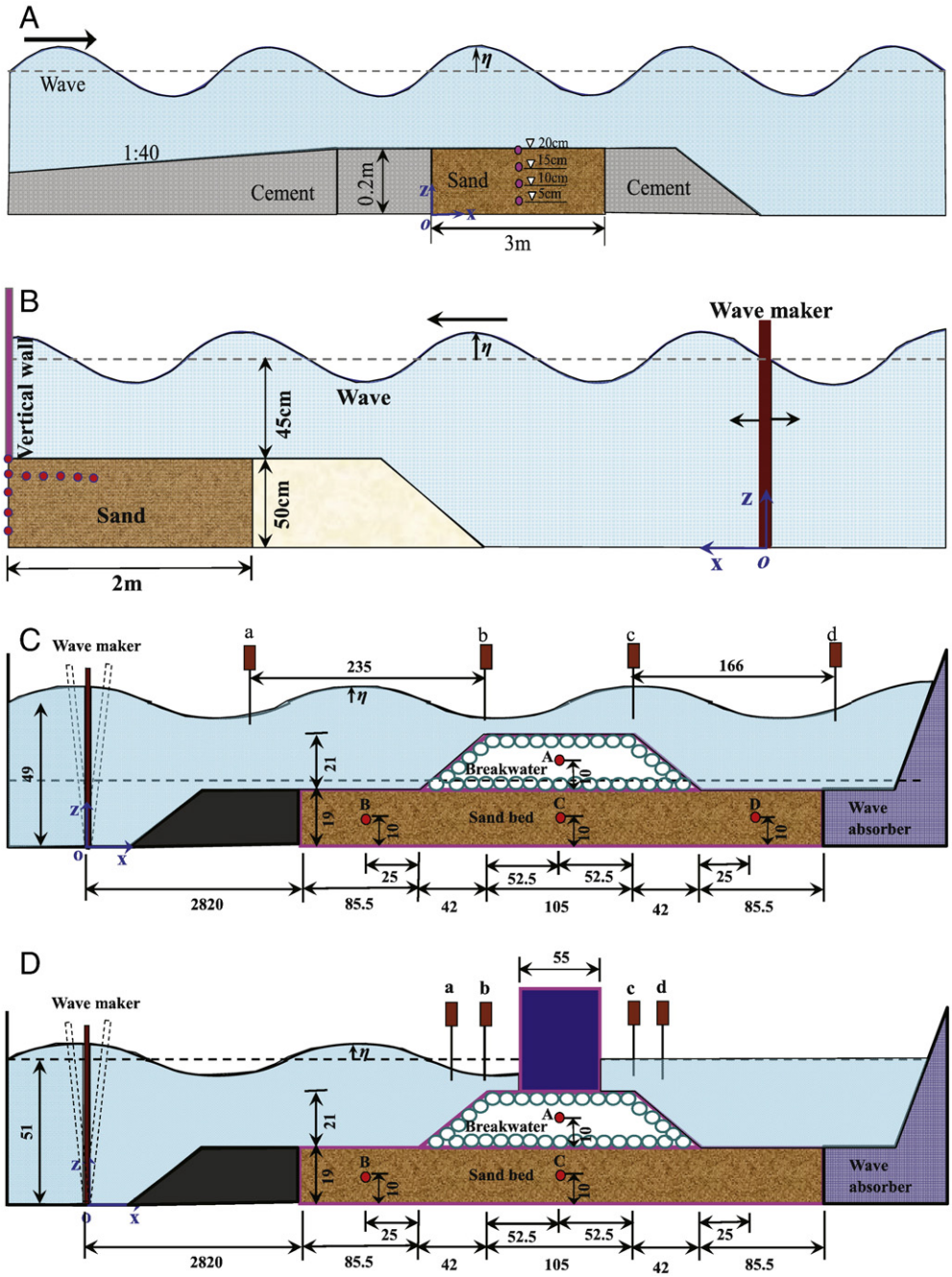

Fig. 3. Experiment setup of previous wave tank experiments for the validation of the present model. (a) Lu's (2005) experiment — fifth-order wave and cnoidal wave. (b) Tsai and Lee's (1995) experiment — standing wave. (c) Mizutani and Mostafa's (1998) experiment — submerged breakwater. (d) Mostafa et al.'s (1999) experiment — composite breakwater.

Table 1
Soil properties and wave characteristics in verification cases.

Experiments	Wave type	Medium	H (cm)	d (m)	T (s)	G (N/m^2)	μ_s	k_s m/s	n	d_{50} (mm)	S_r
Lu's (2005) experiment	5th-order	Wave	12.0	0.4	1.2						
		Sand bed				1.0×10^7	0.3	1.0×10^{-3}	0.3893	0.44	0.98
Tsai and Lee's (1995) experiment	2nd-order	Wave	5.1	0.45	1.5						
		Sand bed				2.64×10^7	0.3	1.2×10^{-4}	0.38	0.187	0.98
Mizutani and Mostafa's (1998) experiment	Linear	Wave	3.0	0.3	1.4						
		Sand bed				5.0×10^8	0.33	2.2×10^{-3}	0.3	1.0	0.99
		Breakwater				1.0×10^9	0.24	1.8×10^{-1}	0.33	30	0.99
Mostafa et al.'s (1999) experiment	2nd-order	Wave	5.0	0.32	2.2						
		Sand bed				5.0×10^8	0.33	2.3×10^{-3}	0.3	0.8	0.98
		Rubble mound				1.0×10^9	0.24	1.6×10^{-1}	0.33	27	0.99

Author's personal copy

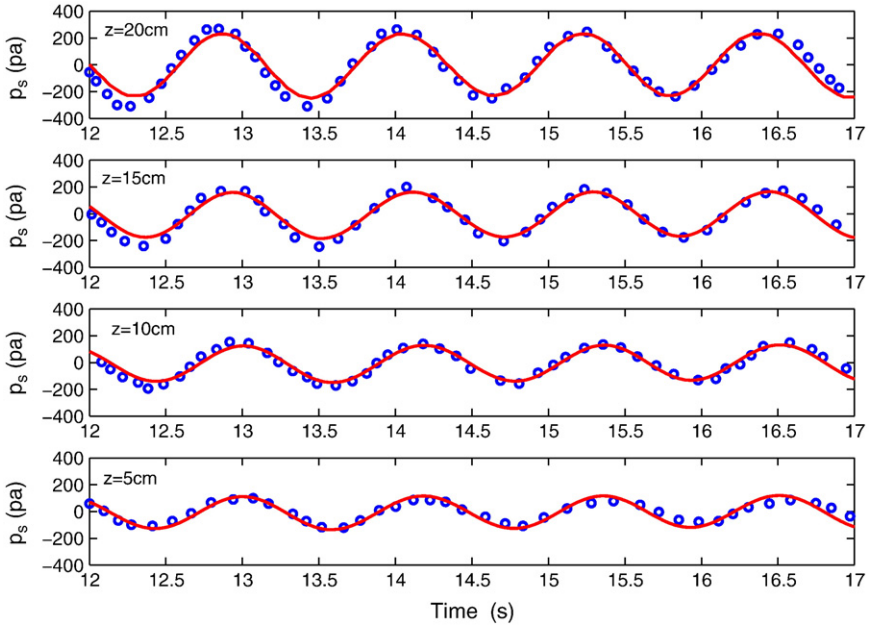

Fig. 4. Comparisons of the wave-induced dynamic pore pressure on the midline of the sand bed between the numerical results and the experimental data in Lu's experiments. — : numerical results; : experimental data.

an impermeable rigid bottom, zero displacement and no vertical flow occur at the horizontal bottom, i.e.,

$$\frac{\partial p_s}{\partial z} = 0 = u_s = v_s \quad \text{at} \quad z = 0. \tag{10}$$

In this study, the finite element model (SWANDYNE II), originally developed by Chan (1988) for the soil dynamic response under earthquake loading, is adopted for the seabed response under wave loading. Details of the generalized FEM formulations are available in Jeng and Ou (2010) and Ye and Jeng (2011). The new feature of the present model is the integration of the wave model with SWANDYNE II to form a new numerical model PORO-WSSI II.

2.3. Integration of the wave and seabed models

In the process of integrating the VARANS equations and the dynamic Biot's equations, two types of the mesh system (matching mesh and non-matching mesh) could be adopted in the numerical computations. In the numerical models proposed by Mizutani and Mostafa (1998) and Mostafa et al. (1999), the matching mesh system is used, in which the same numbers of nodes are required along the sea floor because they have to share the same nodes along the surface of the seabed and marine structures. However, the size of the elements in the fluid domain is generally much smaller than that in the solid domain. The ratio of the size of the elements in the solid domain to that in the fluid domain could vary between 5 and 20. Therefore, the non-matching mesh system is used in this study. To integrate the wave and seabed models together at the interface with the non-matching mesh system, a data exchange port between the VARANS equations and the dynamic Biot's equations is required, in which the radius point interpolation method proposed by Wang et al. (2004) is adopted to implement the data exchange between the wave and soil models.

In the integrated model, to handle the interactions between the wave, seabed and marine structures, the Navier–Stokes equations for the wave and porous flow, and the dynamic Biot's equations for the porous seabed have to be combined together through the continuity of pressure at the interface between the fluid domain and the porous mediums (Fig. 1). It is noted that there may be an argument on using Biot's poro-elastic model for the simulation of the porous flows in the rubble-mound. However, due to the granular material properties, the pore pressures in the rubble-mound predicted by the Biot's model and the VARANS model are close (as demonstrated in the examples presented in the latter sections). Furthermore, the main purpose of using the Biot's model for the rubble-mound is to ensure the continuity of the pressure field between the fluid domain and the porous structures. Therefore, the present approach can provide a good estimation of the pressure filed for engineering practice.

In the computation, the wave model is responsible for the simulation of the wave propagation and the porous flow in the porous structures (seabed, rubble mound and breakwater etc.); and determines the pressure acting on the seabed and marine structures. Due to the fact that the VARANS equations are coupled at the interface between the fluid domain and the porous structures through the pressure and velocity/flux continuity, the pressure and the flow field are continuous in the whole computational domain. Meanwhile, the pressure/force acting on the seabed and marine structures determined by the wave model is provided to the soil model through the data exchange port developed to calculate the dynamic response of the seabed and marine structures, including the displacements, pore pressure and the effective stresses. The details of the process are illustrated in Fig. 2. As shown in the figure, there is no feedback loop in the proposed integrating process, even when the seabed deforms. The proposed process is only valid to the cases with a small deformation of the seabed. Liu et al. (2007) proposed a coupled model for the interaction between the wave and the pore water in the seabed, in which the Navier–Stokes equation for the wave motion on the seabed, and Darcy's flow for the pore water in the seabed are used. The pressure and velocity continuity at their interface are implemented for the two models; namely it is a two-way coupling. However, the limitation of this method is that the effective stresses in the seabed cannot be determined. It is noted here that although the VARANS equation and Biot's equation are only integrated together in this study, the flow field determined by the VARANS equation is continuous in the whole computational domain because the porous medium, such as the rubble mound, and the seabed are all considered as porous structures in the wave model.

Author's personal copy

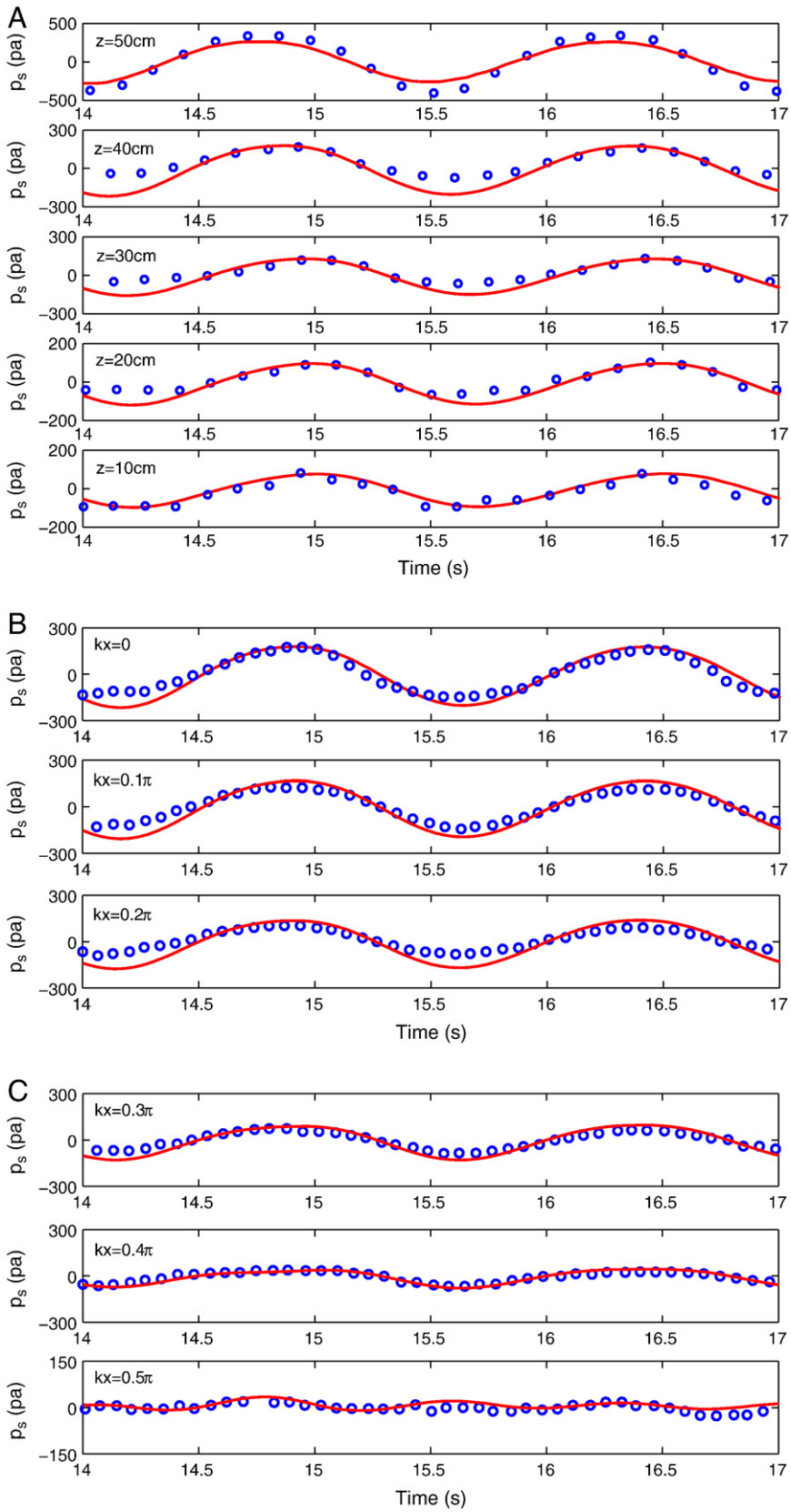

Fig. 5. Comparisons of the standing wave-induced dynamic pore pressure in the sand bed in Tsai and Lee's (1995) experiment. — : numerical results, : experimental data. (a) Pressure on the left-end-side of sand bed ($x=0$). (b) Pressure on the line parallel with the seabed surface ($x=0.0$–0.2π). (c) Pressure on the line parallel with the seabed surface ($x=0.3\pi$–0.5π).

Author's personal copy

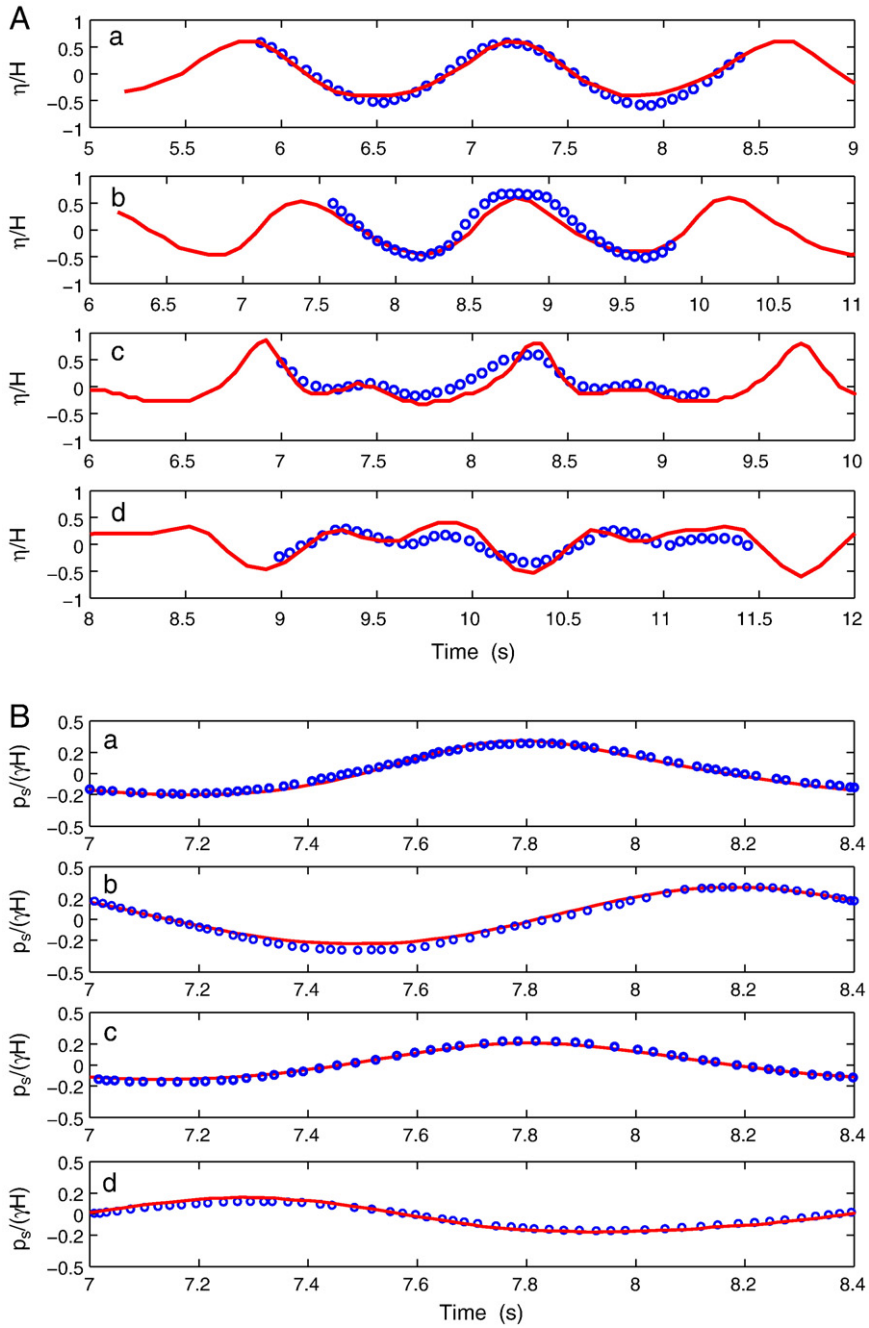

Fig. 6. Comparison of (a) the wave profile and (b) the pore water pressure in the seabed between the PORO-WSSI II model and the experimental data in Mizutani and Mostafa (1998). — : numerical results; : experimental data. (a) Wave profile. (b) Pore water pressure.

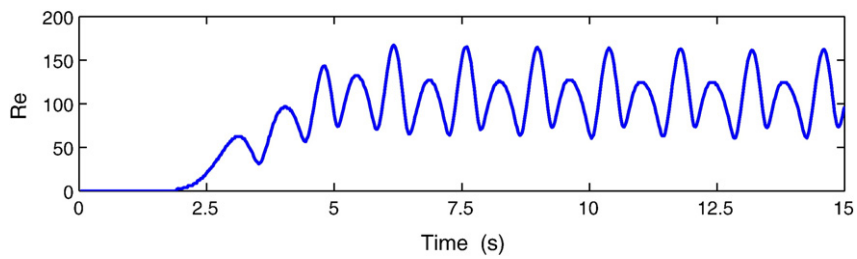

Fig. 7. The variation of the Reynolds number ($Re = \frac{\sqrt{u_R^2 + u_D^2}\, d_{50}}{\nu}$) of the porous flow at $x = 4.715$ m, $z = 0.2905$ m in the rubble mound.

Author's personal copy

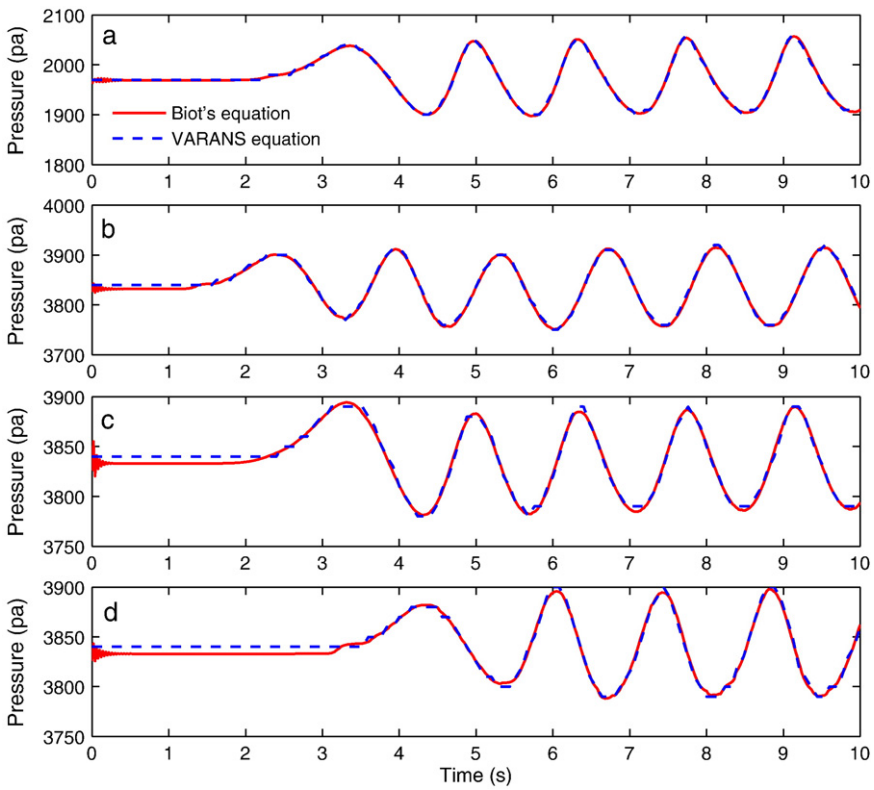

Fig. 8. Comparison of the pore pressure determined by the Biot's equation and the VARANS equation in the rubble mound and sandy bed.

3. Verifications

To validate the proposed numerical model, four sets of the previous experiments available in the literature are used. The experimental set-up of these experiments is given in Fig. 3. The input data of all experiments are tabulated in Table 1.

3.1. Lu's (2005) experiment-progressive waves

Lu (2005) conducted a series of laboratory experiments for the wave-induced dynamic response of sand bed in a wave flume, which is 60 m long, 1.5 m wide and 1.8 m high. The waves generated in the wave flume include regular progressive waves and cnoidal waves. The periods of the wave vary from 1.0 to 1.8 s and the wave heights vary from 8 to 16 cm. The experiment setup is shown in Fig. 3(a). The pore pressure at the four points on the midline of the sand bed is measured in experiments. In the present model, the 5th-order Stokes wave theory is adopted for the generation of the regular progressive wave ($H=$ 12 cm, $d=0.4$ m, $T=1.2$ s). As illustrated in Fig. 4, the numerical prediction of the wave-induced pore pressures overall agrees well with the experimental data (Lu, 2005).

3.2. Tsai and Lee's (1995) experiment-standing wave

Another set of experiment for the validation was conducted by Tsai and Lee (1995) in a wave flume for a standing wave system. As shown in Fig. 3(b), the wave generated by the wave maker propagates into the sand bed region, and to the vertical smooth wall, from which a perfect reflection of the wave occurs. In the sandy bed, the wave-induced pore pressure at 9 points were measured (shown in Fig. 3(b)). Among these, five measurements are taken on the left-end-side of the sand bed, four are on the line parallel with the seabed surface, and the distance to the seabed surface is 10 cm. The intervals between the ten points are 10 cm. As shown in Fig. 5, the present model overall agrees with the experimental data. Some differences for the minimum pore pressure between the present model and the experimental data are observed at the upper four points on the left-end-side of the sand bed (Fig. 5(a)), and the left four points on the line parallel with the sand bed surface (Fig. 5(b) and (c)).

3.3. Mizutani and Mostafa's (1998) experiment — submerged breakwater

The third set of comparison is with Mizutani and Mostafa (1998), in which a series of the wave flume experiments was conducted to investigate the interaction between the regular wave, submerged breakwater and sand bed. The experiment setup is shown in Fig. 3(c). In the experiment, a submerged breakwater is constructed on the sand bed. Four wave gages are installed at points *a*, *b*, *c* and *d* to monitor the wave profile. Four pressure sensors are installed at points A, B, C and D to record the pore pressure. The properties of the sand bed and breakwater, and the wave characteristics provided by Mizutani and Mostafa (1998) are listed in Table 1. Due to the fact that the wave steepness is 0.0143, the linear wave model is enough to accurately simulate the generation and propagation of the wave in the wave flume.

The present integrated model (PORO-WSSI II) is adopted to simulate the interaction between the regular wave, submerged breakwater and sand bed. In the computation, the sand bed and breakwater are treated as different porous structures in the fluid domain in the wave model. The data exchange is implemented by the integrating algorithm at the interface between the solid domain (sand bed, breakwater) and the fluid domain. In the soil model, the sand bed and breakwater are also treated as different porous mediums with different properties (see Table 1).

The comparisons for the wave profile and the wave-induced dynamic pore pressure in a sand bed and rubble mount breakwater between the numerical results predicted by the present model and the experiment data are shown in Fig. 6. As illustrated in the figures, the agreements

Author's personal copy

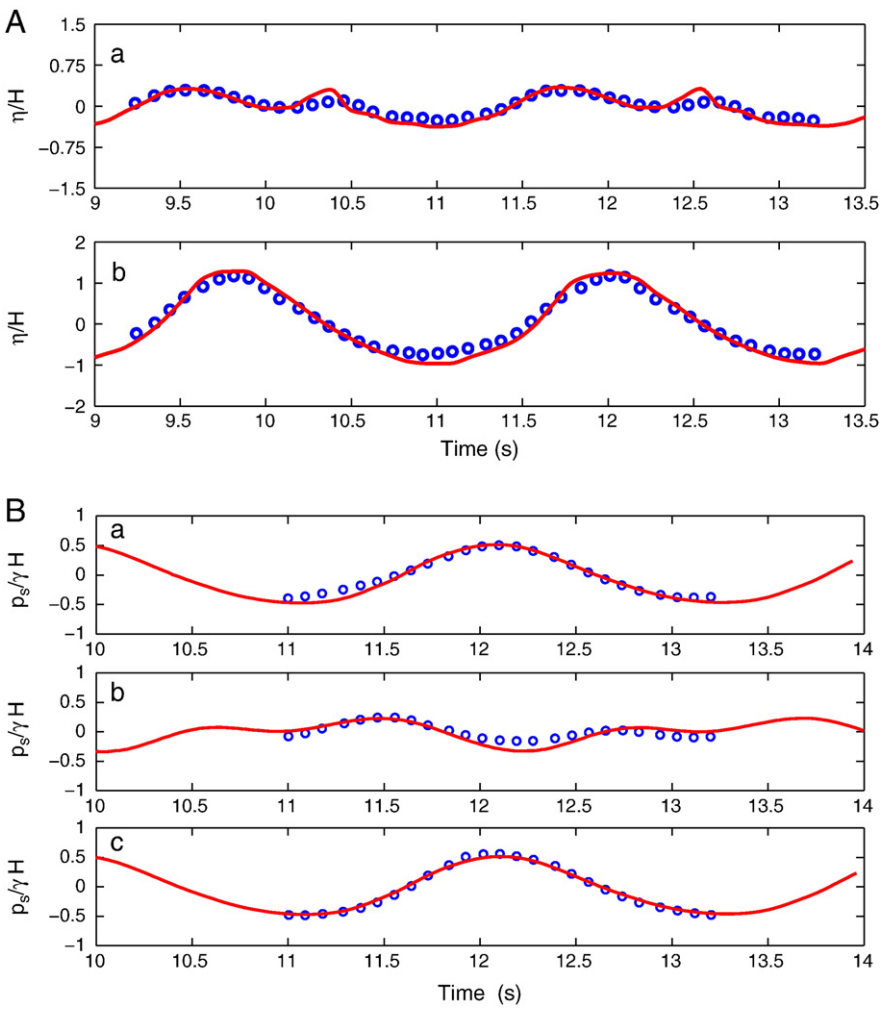

Fig. 9. Comparison of (a) wave profile and (b) pore water pressure in the seabed between the PORO-WSSI II model and the experimental data in Mostafa et al.(1999) for the wave profile. — : numerical results; : experimental data. (a) Wave profile. (b) Pore water pressure.

for the wave profile at *a* and *b* are good, while, some little differences are observed at points *c* and *d* that are located behind the breakwater. Furthermore, the agreements for the wave-induced dynamic response at A, B, C and D are all excellent. The comparison clearly demonstrates that the integrated model PORO-WSSI II is applicable for the WSSI problems.

Here, a problem about the application of Biot's equation for the turbulent porous flow in the porous medium with very high permeability is worth discussing. Biot's equation is established based on the assumption of laminar flow (Darcy's flow) in the porous medium. In this verification case, the permeability of the submerged breakwater is high (0.18 m/s); and the mean particle size is relatively large (30 mm). It is interesting

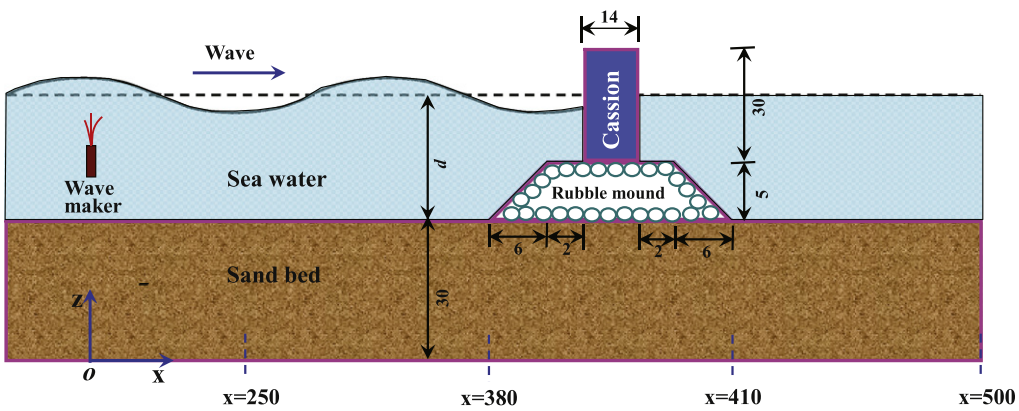

Fig. 10. The sketch of the wave–seabed interaction around a composite breakwater (unit: m).

Author's personal copy

Table 2
Properties of seabed soil, rubble mound and caisson adopted in the large-scale model.

Medium	G (kN/m^2)	μ_s	k_s m/s	n	d_{50} (mm)	S_r
Seabed soil	1.0×10^5	0.33	0.0001	0.25	0.5	98%
Rubble mound	5.0×10^5	0.33	0.2	0.35	400	98%
Caisson	1.0×10^7	0.25	0.0	0.0		0%

to illustrate whether Biot's equation can predict the wave induced porous flow in the rubble mound as the VARANS equation. Through the computation using the VARANS equation, it is found that the velocity of pore water in the submerged rubble mound breakwater is in the magnitude of $O(10^{-1})$ m/s. The Reynolds number $\left(Re=\frac{\sqrt{u_{fx}^2+u_{fz}^2}d_{50}}{\nu}\right)$ can reach up to 180 at the center of the rubble mound (Fig. 7). Fig. 7 indicates that the porous flow in the rubble mound breakwater in this verification case is the laminar flow.

Fig. 8 further presents the comparison of the wave induced pore pressure determined by Biot's equation and VARANS equation at the positions A, B, C and D in the rubble mound and sand bed. Among the four positions, A is located at the center in the rubble mound. In Fig. 8, it is found that the pore pressure at position A determined by VARANS equation and Biot's equation is exactly the same. It is indicated that Biot's equation can be used if the Reynolds number is less than 200 for small-scale cases. It is not surprising that the wave induced pore

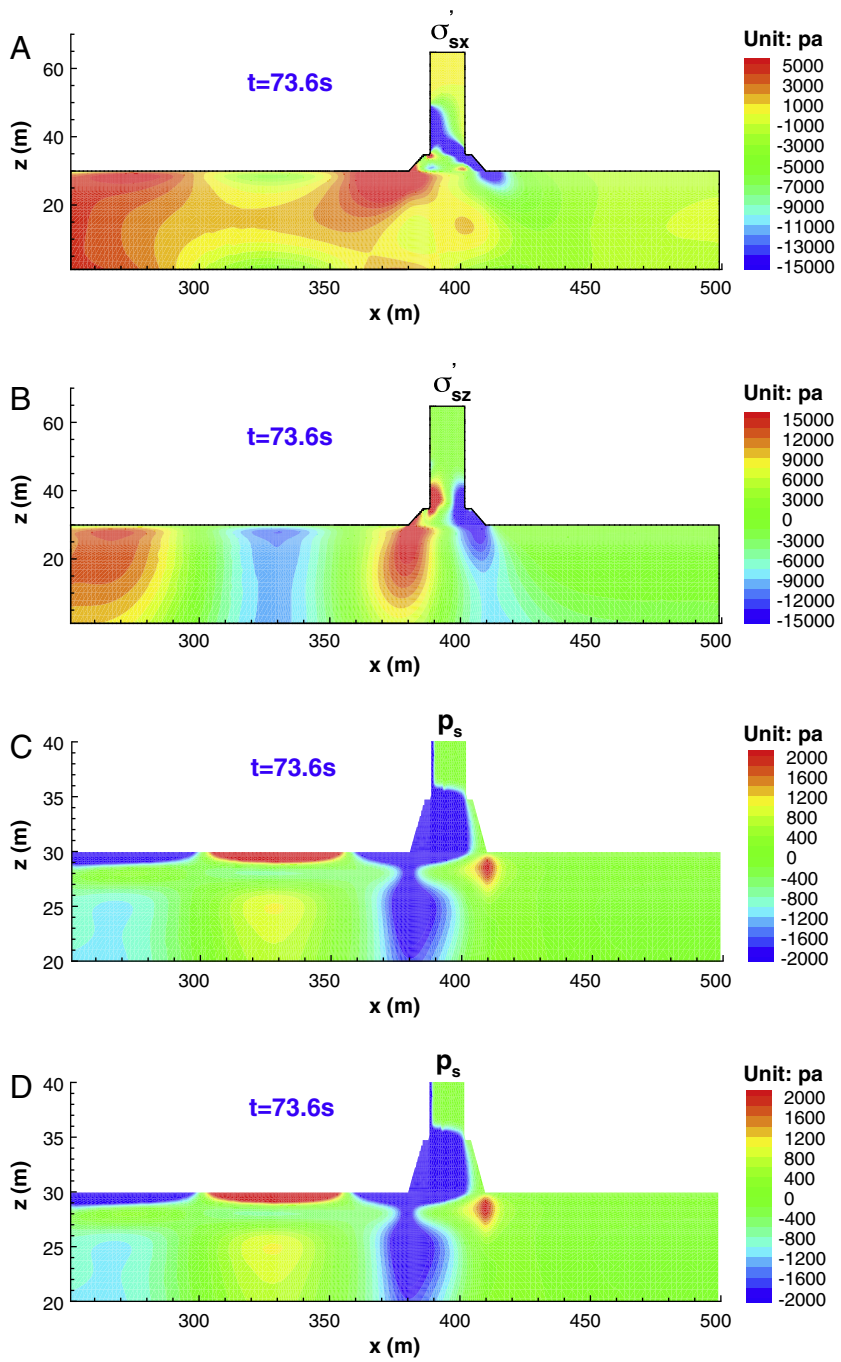

Fig. 11. The distributions of the effective stresses and pore pressure in the seabed and composite breakwater after consolidation under the loading of static water pressure, self-gravity and the gravity of the composite breakwater. The negative value means compressive stress. The static water depth $d=20$ m.

Author's personal copy

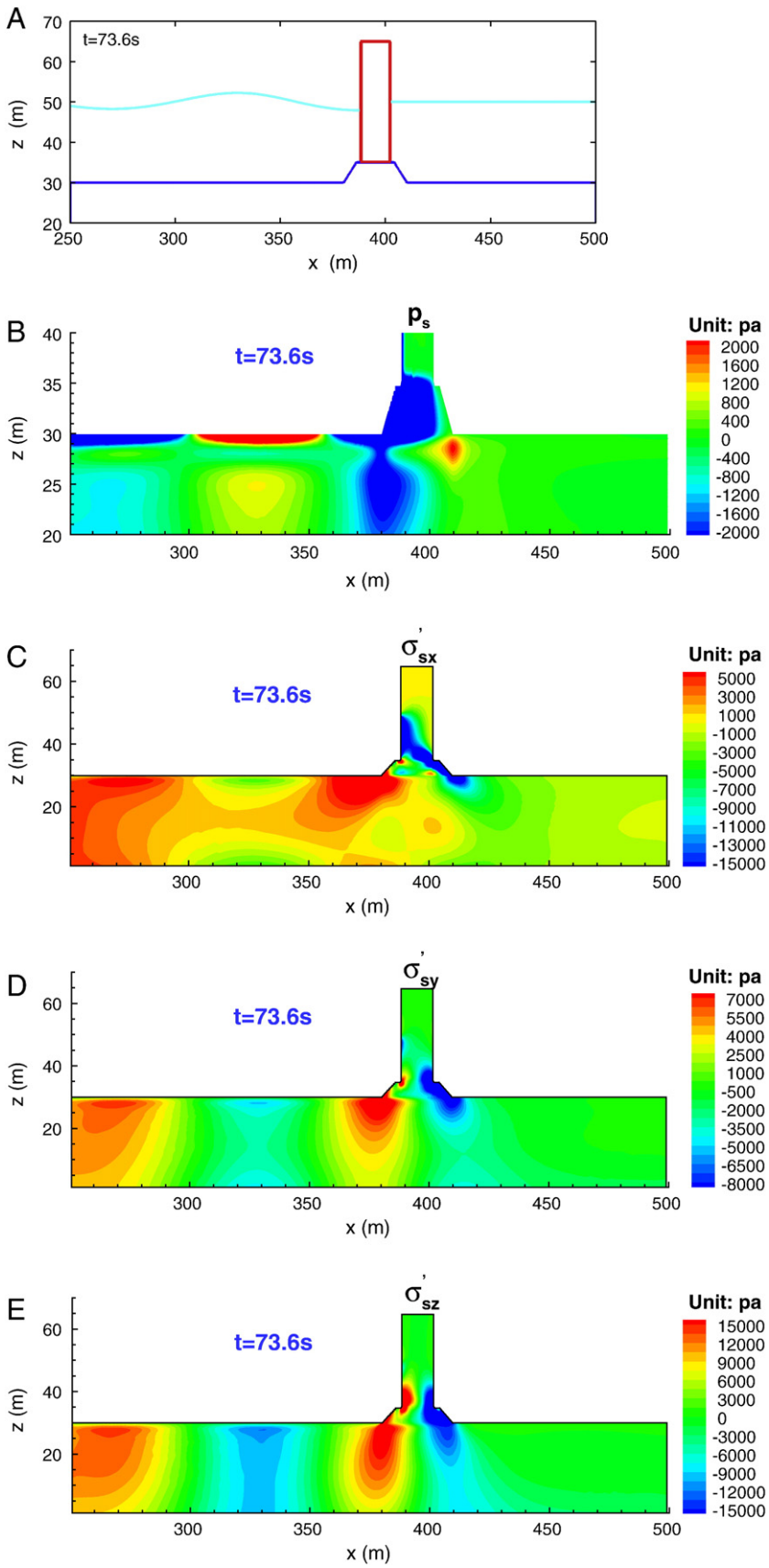

Fig. 12. The dynamic response of the seabed and composite breakwater under the ocean wave loading at $t = 73.6$ s. Wave characteristics: $T = 10$s, $H = 3$ m, $d = 20$ m.

Author's personal copy

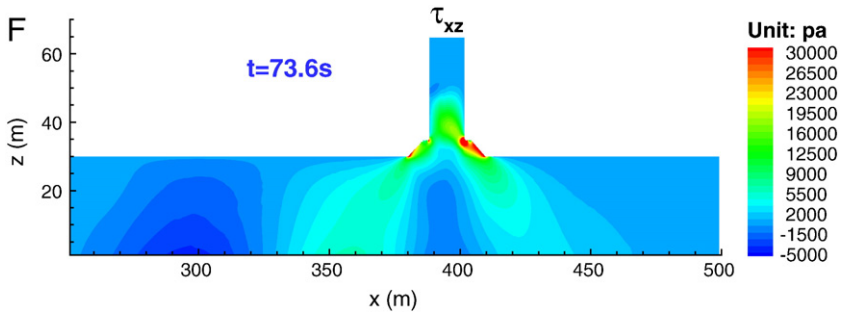

Fig. 12 (*continued*).

pressure at positions B, C and D determined by the two models are the same, because the porous flow in the sand bed with small permeability is the laminar flow.

3.4. Mostafa et al.'s (1999) experiment — composite breakwater

Based on the experiments conducted by Mizutani and Mostafa (1998), Mostafa et al. (1999) further conducted a series of experiments in the same wave flume to investigate the interaction between the wave, composite breakwater and sand bed, as shown in Fig. 3(d). In the experiments, a wooden box (the width is 55 cm) is placed on the breakwater to form a composite breakwater in the wave flume. Four wave gages are installed at points *a*, *b*, *c* and *d* to monitor the wave profile; two of them are in front of the composite breakwater, while the other two are behind the composite breakwater. Three pressure sensors are installed at points A, B and C to record the pore pressure. The properties of the sand bed and breakwater, and the wave characteristics provided by Mostafa et al. (1999) are listed in Table 1. Here, the wave model with a wave maker of the second-order Stoke wave is adopted to simulate the generation, propagation, reflection and interference of wave.

The present model is adopted to simulate the interaction between the wave, composite breakwater and sand bed. In computation, the sand bed and the rubble mound of the composite breakwater are treated as different porous structures in the fluid domain; the wooden box is treated as an impermeable structure in the fluid domain in the wave model. The data exchange is implemented at the interface by the integrating algorithm at the interface between the solid domain (sand bed, rubble mound and wooden box) and the fluid domain. In the soil model, the sand bed and the rubble mound are treated as different porous mediums with different properties, see Table 1; and the wooden box is treated as a rigid and impermeable object located at the top of the rubble mound. It is noted that the buoyancy acting on the bottom of the wooden box applied by the pore water in the rubble mound has been considered in this case.

The comparisons for the wave profile and the wave-induced dynamic pore pressure in the sand bed and the rubble mound between the numerical results predicted by PORO-WSSI II and the experiment data are shown in Fig. 9. Due to the blocking effect of the impermeable wooden box, only little water can flow into and out the right side of the composite breakwater through the rubble mound. Therefore, the amplitude of the wave behind the composite breakwater is very small. In Fig. 9(a), only the wave profiles of points *a* and *b* are used to make the comparison

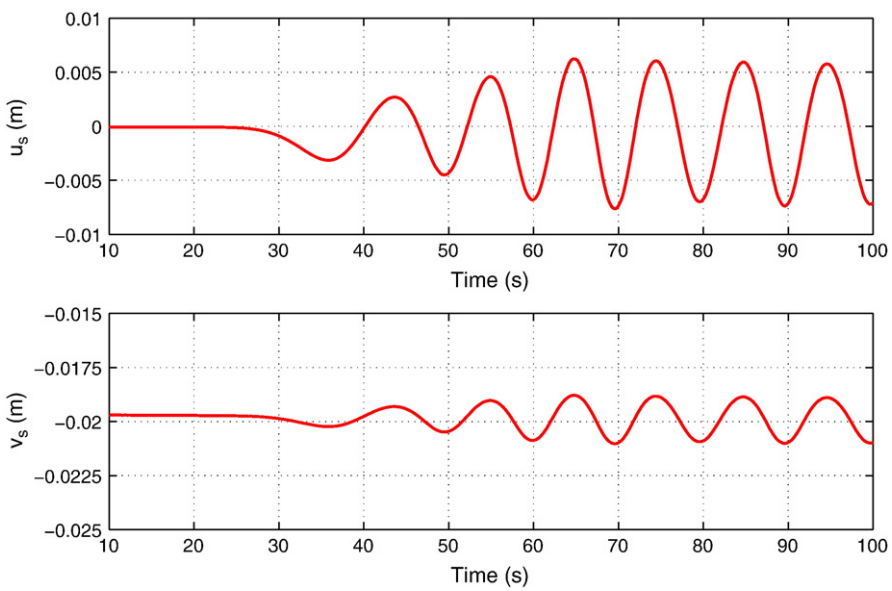

Fig. 13. The variation of horizontal and vertical displacements on the left corner of the impermeable caisson under the ocean wave. The negative value of "u_s" means moving toward left, the negative value of "v_s" means moving toward down.

Author's personal copy

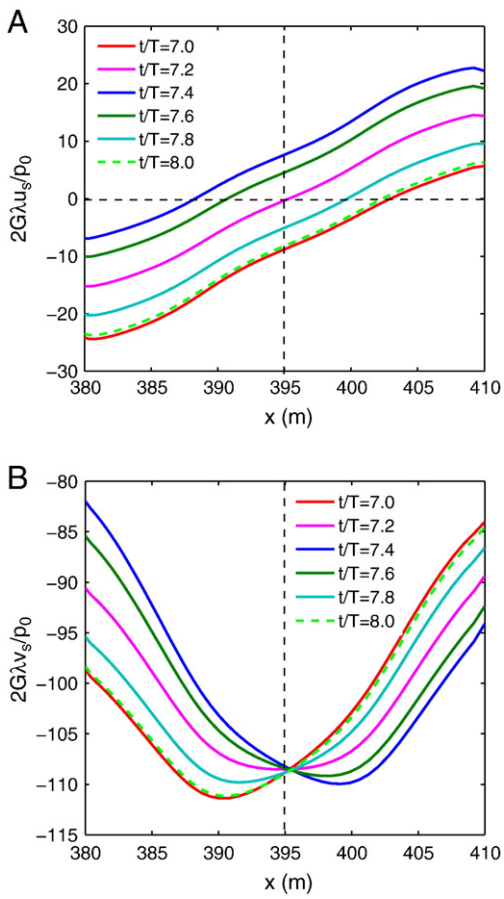

Fig. 14. Distributions of the horizontal and vertical displacements at the bottom of the rubble mound at different times under the ocean wave loading. λ: wave number, $p_0 = \gamma_\omega H/(2\cosh(\lambda d))$. (a) Horizontal displacement. (b) Vertical displacement.

between the numerical results and experiment data. From the figure, it can be seen that the numerical results obtained by the present model agree well with the experiment data both for the wave profile and the wave-induced dynamic pore pressure.

4. Application: seabed response around the composite breakwater under the ocean wave loading

In this section, the present model (PORO-WSSI II) is applied to investigate the response of the seabed and a composite breakwater under wave loading in real offshore environments. In the examples, we consider a composite breakwater consisting of a permeable rubble mound and an impermeable caisson, sitting on a porous seabed. The thickness of the seabed is 30 m, and the horizontal computational length of the seabed is chosen as 250 m, which is much greater than the horizontal dimension of the composite breakwater. The dimensions and position of the composite breakwater are shown in Fig. 10. In the soil model, a total of 13,450 four-node elements are adopted to discretize the seabed foundation and the composite breakwater. In the range z = 27 m the vertical size of the elements varies from 0.1 m to 0.3 m. In the other range z ≤ 27 m, the vertical size of the elements is 0.8 m to 2.0 m. The horizontal size of the elements in the whole domain is set at 0.5 m to 2.0 m. In the wave model, the horizontal and vertical sizes of the grids are 0.3 m and 0.06 m, respectively. The numerical calculation for the determination of the wave field and the dynamic response of the composite breakwater and its seabed foundation took about 70 h of computation time on the Dell Workstation T7500.

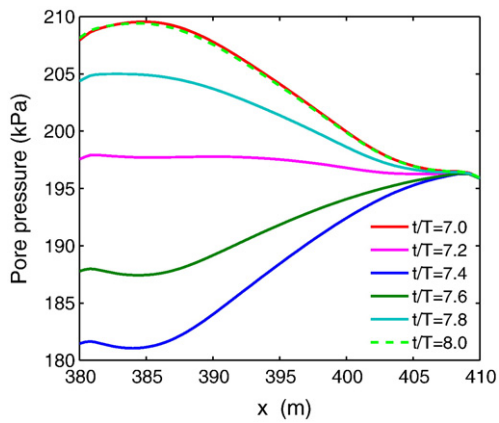

Fig. 15. The distributions of the pore pressure at the bottom of the rubble mound at different times under the ocean wave loading.

4.1. Consolidation of the seabed under composite breakwater and static water pressure

In natural offshore environments, the seabed generally has experienced the consolidation process under the seawater loading and self-gravity in the geological history. In addition, after the composite breakwater is constructed, the seabed in the vicinity of the composite breakwater will be compressed and deformed due to the static loadings. The seabed will then reach a new balanced state, based on the previous consolidation state under dead loading. Therefore, to correctly simulate the interactions between the ocean waves, a seabed and marine structures, the initial consolidation state of the seabed due to static loadings has to be determined before the ocean wave loading is applied in the numerical model. In this section, the initial consolidation state of the seabed is calculated by using the present model (PORO-WSSI II) with the static loadings, including the static water pressures and weight of the composite breakwater. The properties of the seabed soil, rubble mound and caisson are listed in Table 2. The distributions of the effective stresses and pore pressures in the seabed after the pre-consolidation process of the seabed are illustrated in Fig. 11.

As illustrated in Fig. 11, the effective normal stresses ($\sigma'_{sx}, \sigma'_{sz}$) and shear stress ($\tau_{sxz}$) have been significantly affected by the composite breakwater in the seabed foundation, which is in the range between $x = 350$ m and $x = 450$ m. The effective stresses obviously increase due to the weight of the composite breakwater in the seabed foundation. In the region far away the composite breakwater, the influence of the structure on the effective stresses vanish. Fig. 11 shows that the pore pressure in the rubble mound and the seabed increase uniformly from the top of rubble mound to the bottom of the seabed; the pore pressure in the caisson is zero due to that it is an impermeable medium. It is noted that there is an upward buoyancy acting on the bottom of the caisson applied by the seawater.

4.2. Dynamic response of the seabed

Once the initial consolidation state of the seabed is determined under the static water pressure and weight of the composite breakwater, it will be taken as the initial stress state when determining the dynamic response of the seabed under dynamic ocean wave loading. As shown in the procedure (see Fig. 2), the seabed and the rubble mound are considered as the porous medium, while the caisson is considered as the impermeable structure in the wave model. The full pressure acting on the sea floor and the composite breakwater is transmitted to the soil model that is used to predict the response of the seabed and the composite breakwater. The predicted seabed responses induced by the full pressure

Author's personal copy

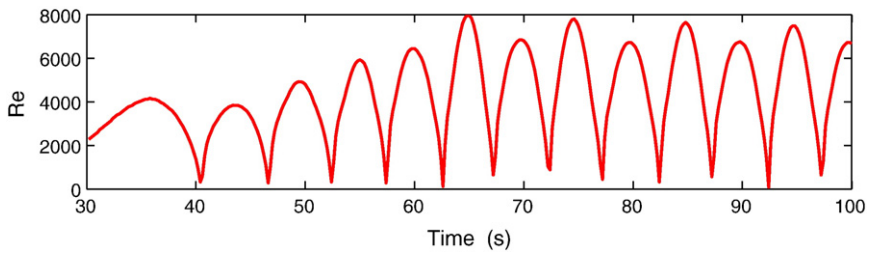

Fig. 16. The variation of the Reynolds number ($Re = \frac{\sqrt{u_x^2+u_z^2}\,d_{50}}{\nu}$) of the porous flow at $x = 395$ m, $z = 32.5$ m in the rubble mound.

are considered as a full response, and the wave-induced dynamic response can be determined from the difference between the full response and the initial consolidation state.

In this example, the wave characteristics are chosen as: wave period $T = 10$s, wave height $H = 3$ m, and water depth $d = 20$ m. Fig. 12 shows the distributions of the dynamic effective stresses and pore pressure in the seabed and the composite breakwater at $t = 73.6$ s under the dynamic wave loading. According to the momentary liquefaction mechanism, the seabed soil will be liquefied when the total stresses become zero in the region, resulting in the failure of the foundations in the vicinity of the marine structures. At the right-hand-side of the composite breakwater, the effect of the ocean wave is limited in a range which does not excess $x = 450$ m due to the blocking of the breakwater. In the region far away from the composite breakwater, the effect of the ocean wave basically disappears. At time $t = 73.6$ s, as shown in Fig. 12, the seabed near the rubble mound is likely to be liquefied when the wave trough is propagating on it, and the dynamic effective stresses and the pore pressure are negative, which would lead to the collapse of the composite breakwater.

Before the ocean wave arrives at the structure, the composite breakwater gradually moves downward to the seabed due to its weight and reaches the initial consolidation state. Fig. 13 shows the development of the horizontal and vertical displacements of the upper left corner of the caisson. The results indicate that the structure vertically subsides about 19 mm during $0 < t < 25$ s. After the ocean wave reaches the caisson ($t > 25$ s), the caisson begins to vibrate vertically and horizontally with a small amplitude. After the full interaction of the wave and the structure ($t > 60$ s), the breakwater subjects to a periodical wave force and its induced vibration.

Fig. 14 illustrates the distributions of the horizontal and vertical displacements around the bottom of the rubble mound at different time levels after the standing wave system is fully developed. It is found (graphs not shown) that the horizontal and vertical displacements at the bottom of the rubble mound are both symmetric in the first two wave periods. There is no further movement before the ocean wave reaches the composite breakwater. After the 4th wave crest has arrived, the horizontal and vertical displacements at the bottom of the rubble mound begin to gradually increase with a small magnitude due to the loading of the ocean wave. When the interaction between the ocean wave and the composite breakwater becomes much more intensive, the displacements at this plane start to increase (see Fig. 14).

Fig. 15 shows the distribution of the pore fluid pressure around the bottom of the rubble mound after the standing wave system is fully developed. The numerical results show that the pore pressure beneath the rubble mound is a little higher than that outside of the rubble mound in the 2nd period. In the 4th period, the pore pressure begins to vary due to the wave motion around the composite breakwater. When the wave crest arrives at the composite breakwater, the pore pressure on the bottom of the rubble mound increases; while the pore pressure decreases with the wave tough above. The impact of the wave motion on the pore pressure near the right end of the bottom of the rubble mound ($x = 407$–410 m) becomes negligible, indicating that the breakwater can efficiently protect the offshore seabed and coastline from the erosion by the ocean wave.

In the verification case related to Mizutani and Mostafa (1998), it is demonstrated that Biot's dynamic poro-elastic theory is applicable for the cases with the Reynolds number (Re) of less than 200 for small-scale cases. Here, it is also interesting to examine the applicability of Biot's dynamic model for large-scale cases. In this section, the composite breakwater consists of a rubble mound and a caisson. The mean particle size of this rubble mound is 400 mm, and its permeability is 2.0×10^{-1} m/s. Undoubtedly, the wave induced flow in the rubble mound is turbulent due to that fact the magnitude of the velocity of the pore water reaches up to 0.6 m/s. Fig. 16 shows the variation of the Reynolds number of the porous flow at the center point ($x = 395$ m, $z = 32.5$ m) of the rubble mound. It is shown that the Reynolds number of the porous flow in the rubble mound reaches up to 8000. Fig. 17 shows the comparison of the pore pressure at the center of the rubble mound as determined by Biot's equation and VARANS equation, respectively. As illustrated in Fig. 17, the pore pressure at the center of the rubble mound is basically the same. After some intensive parametric study, it is found that Biot's equation can be used for turbulent porous flows when the magnitude of velocity is $O(10^{-1})$ m/s or the Reynolds number is less than 10,000 in large-scale cases.

It well known that Biot's equation includes consolidation equation (Biot, 1941), "$u-p$" approximation (Zienkiewicz et al., 1980) and fully dynamic equation (Biot, 1956). For the turbulent porous flow,

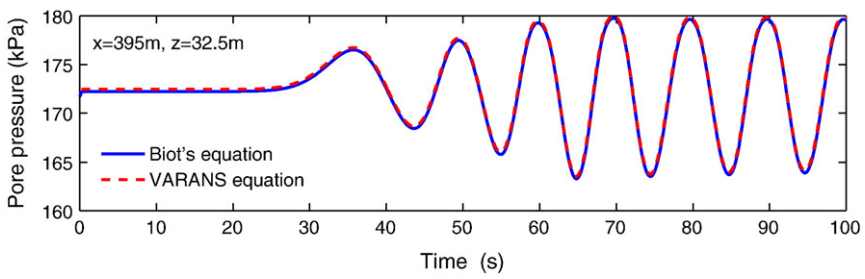

Fig. 17. Comparison of the pore pressure at $x = 395$ m, $z = 32.5$ m in the rubble mound determined by the Biot's equation and the VARANS equation.

Author's personal copy

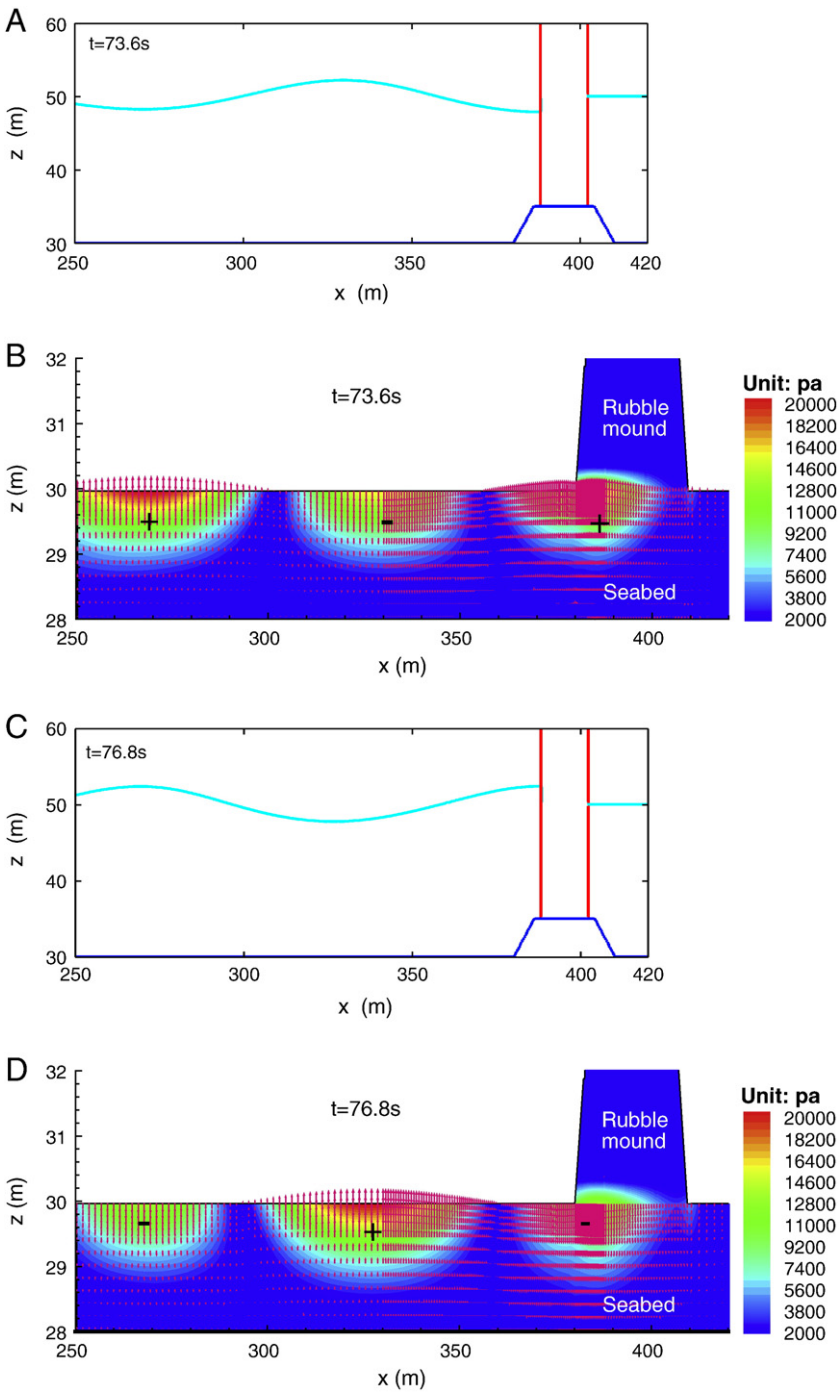

Fig. 18. The seepage force in the seabed under the ocean wave loading at $t=73.6$ s and $t=76.8$ s. "+": upward seepage force, "−": downward seepage force.

the consolidation equation is not applicable because the effect of acceleration of the pore water cannot be ignored under this situation. The "$u-p$" approximation or fully dynamic equation must be used for turbulent porous flows in computation.

4.3. Wave-induced liquefaction

Two mechanisms of the wave-induced soil response have been observed in the laboratory and field measurements, depending on the manner that the pore pressure is generated (Zen and Yamazaki, 1990). One is caused by the progressive nature of the excess pore pressure, which appears at the initial stage of cyclic loading (Seed and Rahman, 1978; Sumer and Fredsóe, 2002). The other is generated by the oscillatory pore pressure, which is accompanied by the amplitude damping and phase lag in the pore pressure. This type of soil response appears periodically during a storm sequence (Madsen, 1978; Yamamoto et al., 1978). In this study, we focus on the latter mechanism–oscillatory soil response, which will lead to the momentary liquefaction. Some examples for such a liquefaction have been reported in the literature. For example, two laboratory experiments (Choudhury et al., 2006; Zen and Yamazaki, 1990) have been conducted to confirm the existence of the momentary liquefaction of sand bed under wave loading. A long-term field measurement (Mory et al., 2007) also indicated the occurrence of the wave-induced monetary liquefaction near coastal structures.

Author's personal copy

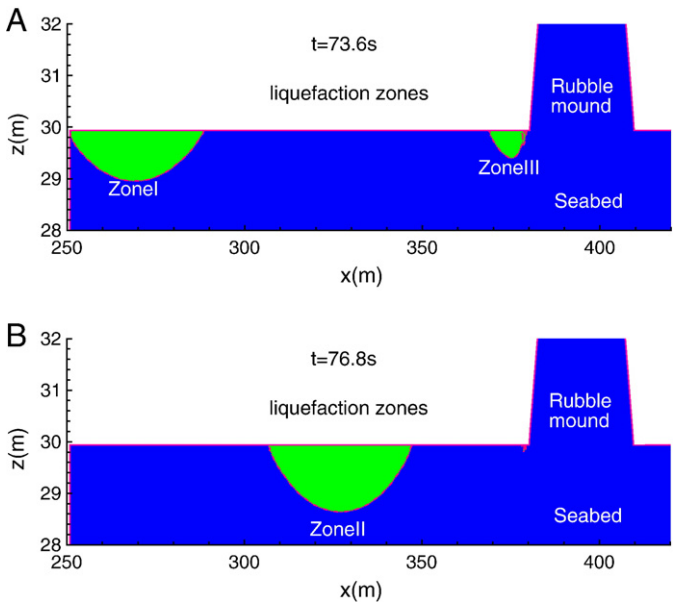

Fig. 19. The three liquefaction zones in the seabed under the ocean wave at times $t=73.6$ s and $t=76.8$ s.

In general, the momentary liquefaction is directly related to the magnitude and direction of the seepage force. The seabed is likely to be liquefied when the seepage force is upward because it will decrease the contact effective stresses between the soil particles. In contrast, the seabed will absolutely not be liquefied when the seepage force is downward because it will increase the contact effective stresses of soil particles. The seepage forces in the seabed, dependent on the gradient of pore pressure, can be defined as:

$$j_x = \frac{\partial p_s}{\partial x} \quad \text{and} \quad j_z = \frac{\partial p_s}{\partial z}. \tag{11}$$

Fig. 18 shows the distributions of the seepage forces in the vicinity of a breakwater at times $t=73.6$ s and $t=76.8$ s. It can be seen that the vertical component of the seepage force is much larger than the horizontal component. The seepage force is upward under a wave trough, while it is downward under a wave crest.

In this study, to investigate the liquefaction properties in a seabed under the ocean wave loading, the liquefaction criterion proposed by Okusa (1985) are used. It is expressed as:

$$(\gamma_s - \gamma_w)(h-z) \le \sigma'_z \tag{12}$$

where the γ_s is the saturation unit weight of the seabed soil, γ_w is the unit weight of water, z is the depth, σ_z' is the wave-induced vertical dynamic effective stress. Actually, the liquefaction criterion (Eq. (12)) means that the seabed will be liquefied, if the wave-induced vertical dynamic effective stress σ'_z (noted: compressive stress is negative) is equal to or greater than the original vertical effective stress $(\gamma_s - \gamma_w)(h-z)$. However, Eq. (12) is only applicable to the cases without a structure. For the cases with a marine structure, it can be modified as:

$$\left|\left(\sigma'_z\right)_{initial}\right| \le \sigma'_z \tag{13}$$

where the $\left(\sigma'_z\right)_{initial}$ is the vertical effective stress at the initial consolidation state.

Fig. 19 shows the liquefaction zones in the seabed under the ocean wave loading at times $t=73.6$ s and $t=76.8$ s, in which the modified liquefaction criterion (13) is adopted. As illustrated in Fig. 19, there are two liquefaction zones in the region near the seabed surface at time $t=73.6$ s; they are located at the range of $250<x<290$ m (Zone I) and $370<x<380$ m (Zone III), respectively. There is only one liquefaction zone in the region near the seabed surface at time $t=76.8$ s, which is located at the range of $310<x<350$ m (Zone II). Zones II and III are very close to the foundation of the breakwater, and they may have a large impact on the foundation stability. Therefore, we will further investigate the (depth, width and area) development of these two liquefaction zones.

Fig. 20 illustrates the variations of the liquefaction potential of Zones II and III under the ocean wave loading ($T=10$s, $H=3$ m, $d=20$ m), respectively. It can be seen from Fig. 20(a) that the liquefaction potential of Zone II is very small when the first wave trough passes through, but it increases largely during the second wave trough. After the interaction between the wave and the structure develops, the liquefaction depth, width and area of Zone II further increase. The maximum liquefaction depth, width and area are about 1.4 m, 41.0 m and 38.5 m^2 (which occur at $t=79$ s), respectively. As shown in Fig. 20(b), the liquefaction potential of Zone III has a similar development process as that of Zone II. The maximum liquefaction depth, width and area of Zone III are about 0.46 m, 11.5 m and 3.85 m^2 (which occur at $t=74$ s), respectively. The liquefaction potential of Zone III is much smaller than that of Zone II, which can be ascribed to the weight of the composite breakwater which significantly increases the vertical effective stress of the initial consolidation state in Zone III.

Although the liquefaction potential in Zone III is small relative to that in Zone II, more attentions need to be paid to the Zone III as it is next to the foundation of the composite breakwater. The soil liquefaction may lead to a collapse of the composite breakwater. In engineering applications, some methods, such as a replacement of the fine sand with gravel material, need to be adopted to protect the structure foundations.

The influence of the inertial terms is associated with the accelerations of the pore water and soil particles on the wave-induced dynamic pore pressure and effective stresses in the previous work (Jeng and Cha, 2003; Ulker and Rahman, 2009; Ulker et al., 2009). It is of interest to examine the effects of the inertial term on the liquefaction potential. In Fig. 20, the predictions of the liquefaction zone by the conventional consolidation model are also included as dashed lines. As shown in the figure, the consolidation model (Jeng et al., 2001) overestimates the liquefaction depth in Zone II, compared with the present dynamic model. However, the predictions of the consolidation model are slightly greater than that of the dynamic model.

It is well known that the wave characteristics, including the wave height (H), wave period (T) and water depth (d) have an impact on the seabed liquefaction. Generally, the seabed is most likely to be liquefied under the long wave with a high wave height propagating in shallow water. In this part, the effect of the wave characteristics on the liquefaction potential is numerically investigated. Only the Zone III is considered here, as this zone is close to the structure foundation and may lead to the foundation instability.

Fig. 21 illustrates the effects of the wave height, wave period and water depth on the maximal liquefaction potential of Zone III. The bench case is with the wave condition $T=10$s, $H=3$ m and $d=20$ m. When investigating the effect of one of the wave characteristics, the other two wave characteristics are kept the same as the bench case. It is shown in Fig. 21 that the wave height, wave period and still water depth all have a great impact on the maximal liquefaction potential in Zone III. A longer wave period, higher wave height or shallower water depth will lead to a larger liquefaction potential. This is mainly due to that the long wave or the wave with a high height carries more energy, leading to a more intensive WSSI. Meanwhile, deep water could effectively reduce the wave-induced dynamic pressure acting on the seabed, and consequently results in the liquefaction potential of the seabed.

In addition to the effects of the wave characteristics, the saturation of the seabed foundation is also an important factor affecting the

Author's personal copy

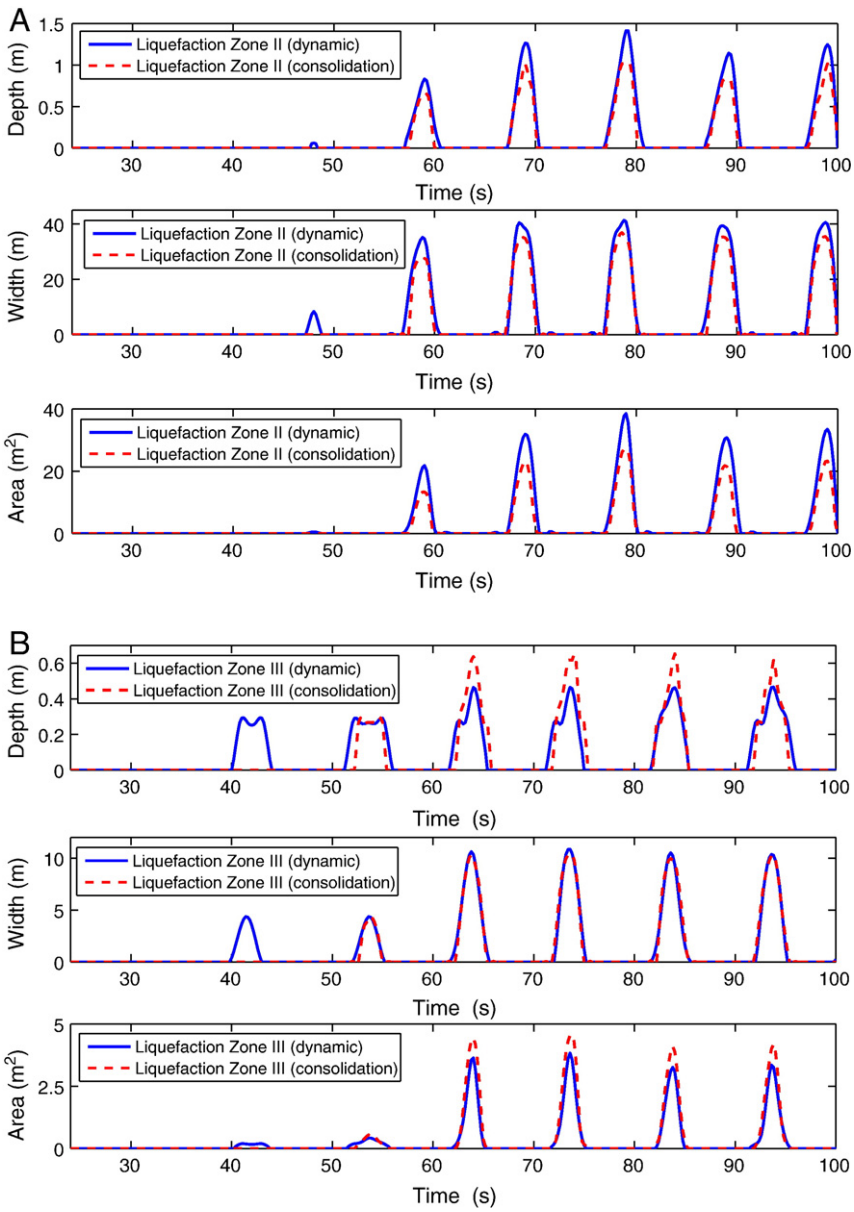

Fig. 20. The liquefaction properties (depth, width and area) in liquefaction Zones II and III.

wave induced transient liquefaction. Under the same wave conditions, the dynamic response of a fully saturated seabed foundation is investigated. It is found that the transient liquefaction does not appear in the saturated seabed foundation (graphs not shown). The reason is attributed to the mechanism of the transient liquefaction in the sand bed: phase lag of the wave induced pressure in the seabed. For the unsaturated seabed, the compressibility of the pore water $1/\beta$ significantly increases compared to that in the fully saturated seabed. The phase lag is positively related to the compressibility of the pore water. Therefore, the phase lag along the depth in the unsaturated seabed is significantly greater than that in the saturated seabed. Correspondingly, the wave induced upward seepage force in the saturated seabed is much less than that in the unsaturated seabed. Therefore, the unsaturated seabed is more likely to transient liquefy under wave loading.

5. Conclusion

In this study, an integrated model (PORO-WSSI II) for the investigation of WSSI is developed. The VARANS equations govern the ocean wave and the porous flow in the seabed and marine structures (wave model), while the dynamic Biot's equations describe the mechanical behavior of the seabed and the marine structures under wave loading (soil model). The integrated model is validated by four laboratory experiments available in the literature. An overall agreement between the present model and the experimental measurements demonstrates the capacity of the present model to predict the behavior of the elastic seabed.

The main advantages of the integrated model include: (1) the complex wave motion in front of the marine structures can be simulated; (2) the effect of the porous seabed and other porous structures on the wave motion, for example wave damping, can be considered; (3) the wave motion and its induced dynamic response of the marine structures and its seabed foundation can be determined simultaneously; (4) the integrated model could be used for the porous flow when the Reynolds number is less than 10,000 for large-scale cases. Based on the above mentioned advantages, the developed integrated model PORO-WSSI II can be a transitive model from the theoretic investigation to practical application.

As an example, PORO-WSSI II is adopted to investigate the interaction between the wave, composite breakwater and its seabed foundation. The numerical results show that there are intensive fluid exchange and

Author's personal copy

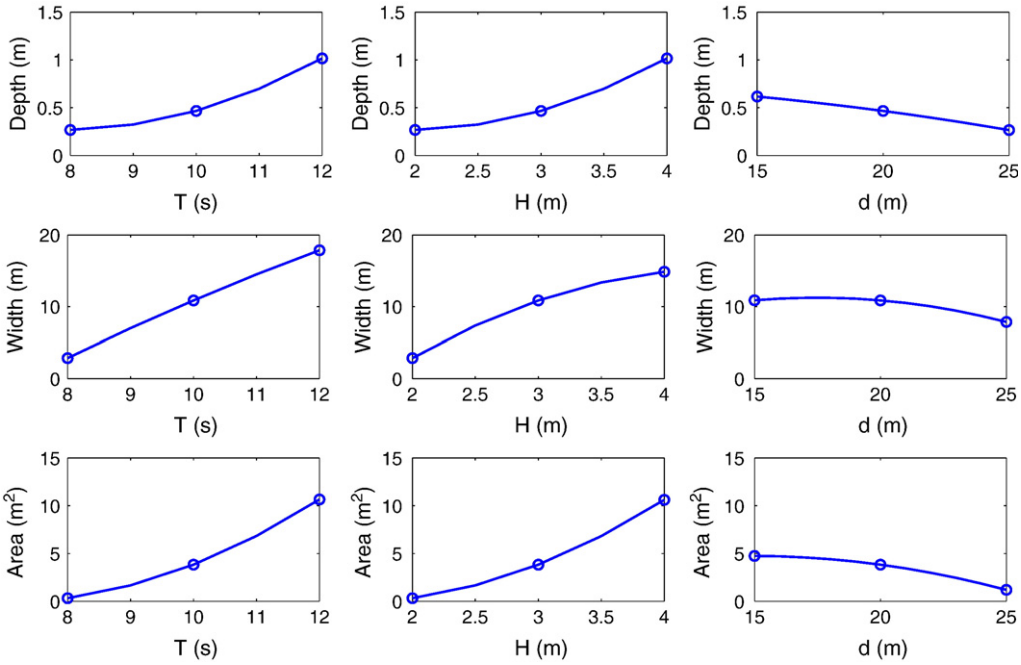

Fig. 21. The effect of the wave characteristics on the liquefaction properties (including maximum liquefaction depth, width and area) of liquefaction Zone III. The standard wave condition is: $T=10$s, $H=3$ m, $d=20$ m.

seepage force in the region close to the seabed surface. The seepage force is upward under wave trough, while it is downward under wave crests. The upward seepage force makes the effective stresses decrease. When the effective stresses decrease to zero, the seabed in the region will be liquefied. As shown in the numerical examples, there are three liquefaction zones near the composite breakwater under the ocean wave loading. Among them, the liquefaction Zone III requires most attention as it is very close to the structure foundation. The wave characteristics (T, H and d) significantly affect the liquefaction potential in the vicinity of the structure (i.e., Zone III). A longer wave period, a higher wave height or shallower water depth will lead to a larger liquefaction potential.

Acknowledgments

The authors are grateful for the financial support from an EPSRC Grant #EP/G006482/1 (UK) and NY Sea Grant Program and National Science Foundation to Cornell University (USA).

References

Biot, M.A., 1941. General theory of three-dimensional consolidation. Journal of Applied Physics 26 (2), 155–164.
Biot, M.A., 1956. Theory of propagation of elastic waves in a fluid saturated porous solid, part II: high frequency range. Journal of Acoustic Society, American 28, 179–191.
Chan, A. H. C., Feb. 1988. A unified finite element solution to static and dynamic problems of geomechanics. Ph.D. thesis, University of Wales, Swansea Wales.
Choudhury, B., Dasari, G.R., Nogami, T., 2006. Laboratory study of liquefaction due to wave–seabed interaction. Journal of Geotechnical and Geoenvironmental Engineering, ASCE 132 (7), 842–851.
Chung, S.G., Kim, S.K., Kang, Y.J., Im, J.C., Prasad, K.N., 2006. Failure of a breakwater founded on a thick normally consolidated clay layer. Geotechnique 3, 393–409.
Franco, L., 1994. Vertical breakwaters: the Italian experience. Coastal Engineering 22 (1–2), 31–55.
Hsu, J.R.C., Jeng, D.-S., 1994. Wave-induced soil response in an unsaturated anisotropic seabed of finite thickness. International Journal for Numerical and Analytical Methods in Geomechanics 18 (11), 785–807.
Hsu, T.J., Liu, T.S.P.L.-F., 2002. A numerical model for wave motions and turbulence flows in front of a composite breakwater. Coastal Engineering 46, 25–50.
Hsu, J.R.C.H., Uda, T., Silvester, R., 2000. Shoreline protection methods — Japanese experience. In: Herbich, J.B. (Ed.), Handbook of Coastal Engineering. McGraw-Hill, New York, pp. 9.1–9.77.
Huang, C.J., Chang, H.H., Hwung, H.H., 2003. Structural permeability effects on the interaction of a solitary wave and a submerged breakwater. Coastal Engineering 49, 1–24.
Hur, D.S., Kim, C.H., Kim, D.S., Yoon, J.S., 2008. Simulation of the nonlinear dynamic interactions between waves, a submerged breakwater and the seabed. Ocean Engineering 511–522.
Hur, D.S., Kim, C.H., Yoon, J.S., 2010. Numerical study on the interaction among a nonlinear wave, composite breakwater and sandy seabed. Coastal Engineering 57 (10), 917–930.
Jeng, D.-S., Cha, D.H., 2003. Effects of dynamic soil behavior and wave non-linearity on the wave-induced pore pressure and effective stresses in porous seabed. Ocean Engineering 30 (16), 2065–2089.
Jeng, D.-S., Ou, J., 2010. 3-D models for wave-induced pore pressure near breakwater heads. Acta Mechanica 215, 85–104.
Jeng, D.-S., Rahman, M.S., 2000. Effective stresses in a porous seabed of finite thickness: inertia effects. Canadian Geotechnical Journal 37 (4), 1388–1397.
Jeng, D.-S., Rahman, M.S., Lee, T.L., 1999. Effects of inertia forces on wave-induced seabed response. International Journal of Offshore and Polar Engineering 9 (4), 307–313.
Jeng, D.-S., Cha, D.H., Lin, Y.S., Hu, P.S., 2001. Wave-induced pore pressure around a composite breakwater. Ocean Engineering 28 (10), 1413–1432.
Lara, J.L., Garcia, N., Losada, I.J., 2006. Rans modeling applied to random wave interaction with submerged permeable structures. Coastal Engineering 53, 395–417.
Lara, J.L., Losada, I.J., Maza, M., Guanche, R., 2011. Breaking solitary wave evolution over a porous underwater step. Coastal Engineering 58 (9), 837–850.
Lin, P., Liu, P.L.-F., 1998. A numerical study of breaking waves in the surf zone. Journal of Fluid Mechanics 359, 239–264.
Liu, P.L.-F., Lin, P., Chang, K.A., Sakakiyama, T., 1999. Numerical modelling of wave interaction with porous structures. Journal of Waterway Port, Coastal and Ocean Engineering, ASCE 125 (6), 322–330.
Liu, P.L.F., Park, Y.S., Lara, J.L., 2007. Long-wave-induced flows in an unsaturated permeable seabed. Journal of Fluid Mechanics 586, 323–345.
Lu, H. B., 2005. The research on pore water pressure response to waves in sandy seabed. Master's thesis, Changsha University of Science & Technology, Changsha Hunan China.
Lundgren, H., Lindhardt, J.H.C., Romold, C.J., 1989. Stability of Breakwaters on Porous Foundation: Proceeding of 12th International Conference on Soil Mechanics and Foundation Engineering, 1, pp. 451–454.
Madsen, O.S., 1978. Wave-induced pore pressures and effective stresses in a porous bed. Geotechnique 28 (4), 377–393.
Mase, H., Sakai, T., Sakamoto, M., 1994. Wave-induced pore water pressure and effective stresses around breakwater. Ocean Engineering 21 (4), 361–379.
Mei, C.C., Foda, M.A., 1981. Wave-induced response in a fluid-filled poro-elastic solid with a free surface — a boundary layer theory. Geophysical Journal of the Royal Astronomical Society 66, 597–631.
Mizutani, N., Mostafa, A.M., 1998. Nonlinear wave-induced seabed instability around coastal structures. Coastal Engineering Journal 40 (2), 131–160.
Mory, M., Michallet, H., Bonjean, D., Piedra-Cueva, I., Barboud, J.M., Foray, P., Abadie, S., Breul, P., 2007. A field study of momentary liquefaction caused by waves around

Author's personal copy

coastal structure. Journal of Waterway Port, Coastal and Ocean Engineering, ASCE 133 (1), 28–38.
Mostafa, A.M., Mizutani, N., Iwata, K., 1999. Nonlinear wave, composite breakwater and seabed dynamic interaction. Journal of Waterway Port, Coastal, and Ocean Engineering, ASCE 125 (2), 88–97.
Okusa, S., 1985. Wave-induced stress in unsaturated submarine sediments. Geotechnique 35 (4), 517–532.
Seed, H.B., Rahman, M.S., 1978. Wave-induced pore pressure in relation to ocean floor stability of cohesionless soils. Marine Geotechnology 3 (2), 123–150.
Shao, S.H., 2010. Incompressible SPH flow model for wave interactions with porous media. Coastal Engineering 57, 304–316.
Sumer, B.M., Fredsóe, J., 2002. The Mechanism of Scour in the Marine Environment. World Scientific, New Jersey.
Travis, J., 2005. Hurricane Katrina: scientists' fears come true as hurricane floods New Orleans. Science 309 (5741), 1656–1659.
Tsai, C.P., Lee, T.L., 1995. Standing wave induced pore pressure in a porous seabed. Ocean Engineering 22 (6), 505–517.
Ulker, M., Rahman, M.S., 2009. Response of saturated and nearly saturated porous media: different formulations and their applicability. International Journal for Numerical and Analytical Methods in Geomechanics 33 (5), 633–664.
Ulker, M.B.C., Rahman, M.S., Jeng, D.-S., 2009. Wave-induced response of seabed: various formulations and their applicability. Applied Ocean research 31 (1), 12–24.
Ulker, M., Rahman, M.S., Guddati, M.N., 2010. Wave-induced dynamic response and instability of seabed around caisson breakwater. Ocean Engineering 37 (17–18), 1522–1545.
Wang, J.G., Zhang, B., Nogami, T., 2004. Wave-induced seabed response analysis by radial point interpolation meshless method. Ocean Engineering 31 (1), 21–42.
Yamamoto, T., Koning, H., Sellmeijer, H., Hijum, E.V., 1978. On the response of a poro-elastic bed to water waves. Journal of Fluid Mechanics 87 (1), 193–206.
Ye, J.H., Jeng, D.-S., 2011. Effects of bottom shear stresses on the wave-induced dynamic response in a porous seabed: PORO-WSSI (shear) model. Acta Mechanica Sinica 27 (6), 898–910.
Zen, K., Yamazaki, H., 1990. Oscillatory pore pressure and liquefaction in seabed induced by ocean waves. Soils and Foundations 30 (4), 147–161.
Zen, K., Umehara, Y., Finn, W.D.L., 1985. A case study of the wave-induced liquefaction of sand layers under damaged breakwater. Proceeding 3rd Canadian Conference on Marine Geotechnical Engineering, pp. 505–520.
Zhang, F.G., Ge, Z.J., 1996. A study on some causes of rubble mound breakwater failure. China Ocean Engineering 10 (4), 473–481.
Zienkiewicz, O.C., Chang, C.T., Bettess, P., 1980. Drained, undrained, consolidating and dynamic behaviour assumptions in soils. Geotechnique 30 (4), 385–395.